GAS SEAL LEAKAGE AT HIGH TEMPERATURE: A LABYRINTH SEAL AND AN ALL-METAL COMPLIANT SEAL OF SIMILAR CLEARANCE

A Thesis

by

ALAIN ANDERSON

Submitted to the Office of Graduate Studies of
Texas A&M University
in partial fulfillment of the requirements for the degree of

MASTER OF SCIENCE

Chair of Committee, Luis San Andrés
Committee Members, Gerald Morrison
Lynn Beason
Head of Department, Andreas A. Polycarpou

August 2013

Major Subject: Mechanical Engineering

ABSTRACT

Reducing secondary leakage is a common challenge in numerous machines, particularly in steam and gas turbines. Too large leakage in seals produces a substantial loss in efficiency and power delivery with an increase in specific fuel consumption. Various seal types exist, each with unique advantages and disadvantages as per leakage, power loss, and wear. Labyrinth seals are most common due to their simple design and low cost. Their main drawback is a too high leakage due to enlarged (worn) clearances when a rotor vibrates.

More complicated seal types, such as brush seals can withstand rotor excursions and ensure lower leakage rates than with labyrinth seals. Brush seals utilize a bristle bed which contacts the rotor and wears out thereby reducing leakage performance. The HALO^{TM} seal, an all-metal seal with flexibly supported shoes, is engineered as a clearance control seal to reduce leakage even more, in particular for operation with high pressure differentials and with high surface rotor speeds.

Static leakage tests with hot air at a high temperature (max. 300°C) conducted in a test rig holding a labyrinth seal and a novel all-metal seal (HALO^{TM} seal), both of the same diameter, length and clearance, show the novel seal leaks ~1/5 the flow of a labyrinth seal for pressure ratios (P_s/P_a) > 3.5. The savings in leakage are maximized during operation at high pressure differentials. Leakage measurements with a rotor spinning to a maximum speed of 2,700 rpm (surface speed = 23.6 m/s) produce a slight decrease in leakage with increasing rotor speed.

The research product is a reliable leakage data base enabling the application of a state of the art sealing technology that increases system efficiency by reducing leakage and extends maintenance intervals by eliminating wear of components.

DEDICATION

To the three people who have been instrumental to my success: my parents, Olga and Oscar Anderson, for their unfailing love, and my younger brother, Oscar Anderson Jr., for his encouragement.

ACKNOWLEDGEMENTS

First and foremost, I would like to express my sincere gratitude to Dr. Luis San Andrés, my advisor and committee chair, for his enormous patience, encouragement, and advice during the development of this research. I also thank him for the opportunity to perform research with the Tribology Group and for broadening my technical skills.

Thanks to Zachary Ashton and Brian Butler for sharing their knowledge on the test rig and instrumentation when I began working on the project. Thanks to James Law, Travis Cable, Kai An, Thomas Chirathadam, Sanjeev Seshagiri, Paola Mahecha, and Ray Mathews for their support and assistance in accomplishing numerous tasks.

Finally, thanks to all my friends and colleagues who made my time at the Turbomachinery Laboratory an enjoyable experience.

NOMENCLATURE

A	πDC_r. Flow area [m^2]
c	$\sqrt{\gamma RT_s}$. Speed of sound [m/s]
C_d	S_{ID}-D. Seal diametrical clearance [m]
C_r	C_d/2. Seal radial clearance [m]
D	Rotor diameter [m]
F	Axial load [N]
H_{ID}	Housing inner diameter [m]
i	Current [A]
$k_{V\omega}$	V/ω. Motor constant [V/(rad/s)]
l	Seal axial length [m]
$\dot{m}$	Mass flow rate [kg/s]
$\wp$	iV. Motor electrical power [W]
P_a	Air absolute ambient pressure [Pa]
P_s	Air absolute supply pressure [Pa]
p_r	P_s/P_a. Pressure ratio
$p_{r,choke}$	Choke pressure ratio
Q	$\dot{m}/\rho$. Volumetric flow rate [m^3/s]
R	Air gas constant [J/(kg-K)]
S_{ID}	Seal inner diameter [m]
S_{OD}	Seal outer diameter [m]
T_a	Ambient gas temperature [K]
T_o	$i \times k_{V\omega}$. Motor torque [N-m]
T_s	Gas temperature [K]
V	Voltage [V]
α	Material linear thermal expansion coefficient [1/K]
δ	$\varphi\sqrt{R}/\sqrt{\gamma}$. Modified flow function
γ	Specific heats ratio = 1.4 for air
Φ	$\dot{m}\sqrt{T}/(P_s D)$. Flow Factor [kg-$K^{0.5}$/(MPa-m-s)]
φ	Flow function [(J/(kg-K))$^{0.5}$]
ρ	$P_s/(RT_s)$. Density [kg/m^3]
ω	Rotor angular speed [rad/s]

TABLE OF CONTENTS

Page

Page

LIST OF FIGURES

Page

Page

Page

Page

LIST OF TABLES

Page

CHAPTER I

INTRODUCTION AND JUSTIFICATION

Parasitic secondary flows (seal leakage) in centrifugal compressors and gas and steam turbines represent a considerable loss of efficiency and power delivery accompanied by an increase in specific fuel consumption [1]. The most common and economical means of reducing secondary leakage are labyrinth seals, even though this seal type wears out with operation and, thereby, reduces performance and could even affect rotordynamic stability [1].

At the other extreme of sealing technology are brush seals which are costlier but commonly used in specialized applications such as aircraft engines and steam turbines. Increases in plant efficiency by as much as 1/6 of a percentage point and with as little as 1/3 leakage as in similar sized labyrinth seals are attributed to brush seals [2].

Other non-contacting seal types, all-metal and compliant, such as finger seals and the Hydrostatic Advanced Low Leakage (HALO^{TM}) seal, are engineered to improve leakage reduction in steam and gas turbines, particularly for operation with high pressure differentials and high tip surface rotor speeds [3].

Siemens Power Generation, Inc., and Advanced Technologies Group, Inc., (ATGI) funded research (2007-2009) to construct a high temperature seal test rig (maximum 300°C) with a rotor turning at low rotational speeds (maximum 26 m/s tip speed). San Andrés and Ashton [4] report the measured leakage performance of various seal types and present comparisons amongst the seals tested. A tested hybrid brush seal showed approximately 38% of the leakage measured in a similar sized labyrinth seal and approximately 61% of the leakage in a similar sized brush seal.

The novel all-metal seal may be better at reducing leakage than a labyrinth seal with a similar axial length because of its unique axial profile which draws the seal towards the disk during pressurization. Therefore, it is essential to conduct a comparison of the measured leakage in a novel seal and the leakage in a three teeth labyrinth seal at various supply pressures, temperatures, and rotor speeds. The results may provide a justification to alter sealing practices by replacing commonly used labyrinth seals with the innovative seal technology.

Seal leakage tests are performed without a motor connection and with a cap placed over the quill shaft to restrict any flow exiting the rear of the test rig. Chapters V and VII detail these tests. On separate tests, a cap is placed in the front of the test rig to quantify the flow resistance of the gap at the rear of the connecting shaft.

Leakage tests with a spinning rotor are performed with various pressures and temperatures for both seals. Chapter VIII describes these tests and presents results. The leakage measurements are corrected by subtracting the (known) flow exiting the rear end of the test rig.

In this thesis, the performance of a three teeth labyrinth seal and an all-metal compliant seal are quantified and compared through measurements of leakage at similar operating conditions. The comparisons determine the suitability of the all-metal compliant seal to reduce leakage in steam and gas turbines, for example. The measurements also provide original equipment manufacturers with a direct comparison of leakage to consider upgrading current seals.

CHAPTER II

LITERATURE REVIEW

Turbomachinery seals are designed to maintain efficiency by minimizing leakage; therefore, seal design is the most cost-effective measure to increase performance by restricting secondary leakage [5]. Operation at high gas temperatures, pressures, and rotor speeds aims to increase efficiency, hence seals must be able to limit flow while enduring rigorous operating conditions [6].

The review details the purpose, usage, and requirements of three types of seals often used in steam and gas turbines; namely, labyrinth seals, brush seals and their variants such as the hybrid brush seal, and a more modern seal type, an all-metal compliant seal with improved leakage characteristics.

Refer to Chupp et al. [1] for a comprehensive review of the purpose and significance of sealing in turbomachinery, particularly in gas and steam turbines. In these applications, mechanical elements sealing secondary flows; i.e., seals to reduce leakage, operate at temperatures up to 600°C, differential pressures up to 21 bar, and withstand surface speeds up to 400 m/s [1]. These extreme operating conditions demand seals with specialized materials and configurations and create particular challenges to establish reliable seal performance and seal life.

Labyrinth seals in gas and steam turbines are an effective and inexpensive method of reducing parasitic secondary flows [5]. As seen in Figure 1, labyrinth seals are clearance (non-contact) seals that permit controlled leakage by dissipating flow energy through a series of cavities. Once the gas traverses a series of cavities, it emerges at the other end of the labyrinth seal at a significantly reduced pressure set by the external conditions [7]. Simple in design, labyrinth seals are adaptable to a wide range of sizes and operating conditions. Labyrinth seals have several disadvantages, including high leakage, damage to components due to particle ingestion, and wear due to intermittent contact with its rotor during startup/shutdown conditions [8]. Importantly enough, labyrinth seals have the potential to generate cross coupled stiffness and negative damping that may induce rotordynamic instabilities. Recent improvements in operating configurations, however, have made labyrinth seals more efficient and less prone to rotordynamic instability [1].

The tooth and cavity geometry and the clearance between the rotor and the tips of seal teeth determine the seal leakage [5]. In practice, the operating clearance increases because of intermittent contact and wear during machine startup and shutdown. In high temperature environments, labyrinth seal designs must also allow for thermal expansion of the rotor and seal.

Childs and Scharrer [9] tested labyrinth seals with teeth on rotor and varying the seal clearance to radius ratios from 4.14×10^{-3} to 7.59×10^{-3}. The authors report that labyrinth seal cross-coupled stiffnesses augment with both increasing clearances and shaft rotational speed. Small clearances may cause damage to the rotor and components by contact, especially at high rotor speeds and with large rotor vibration [10].

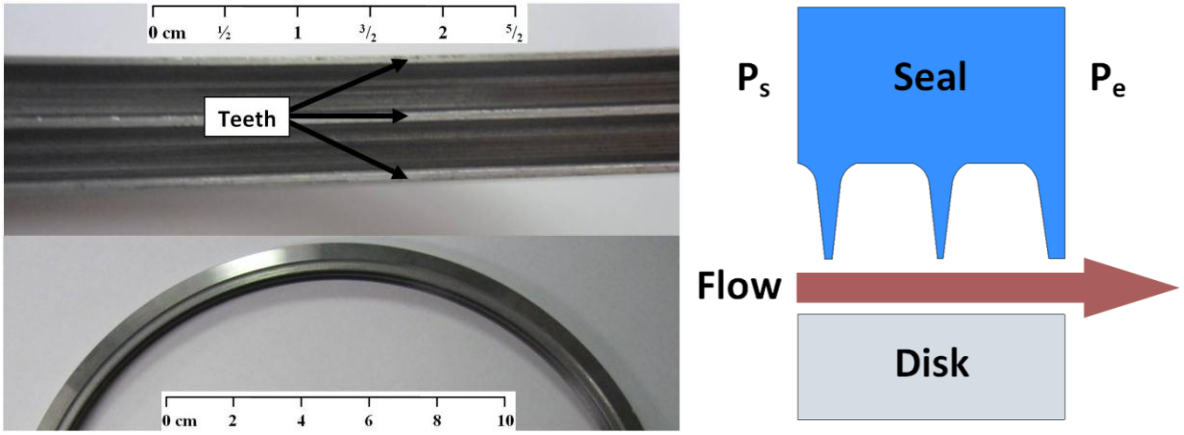

Figure 1. Inner side view of a three teeth labyrinth seal and schematic view of air flow.

The need for improved performance of labyrinth seals led to design modifications such as steps, honeycomb lands, and abradable contact surfaces [2]. With these improvements, the seal teeth operate at lower clearance and with better wear characteristics in the case of radial contact. The wear ultimately rubs the seal inner diameter until an adequate clearance develops. However, these designs work on the principle that a high pressure gas flow is delayed by the presence of a sharp-edged obstruction which leads to a lower pressure in the succeeding cavity. To add flow resistance, additional labyrinths can be placed in parallel thus decreasing further leakage.

Finally, note that labyrinth seals can be manufactured as rings or segmented to facilitate installation, specifically for large land-based gas turbines. As per Floyd [8], there are no

limitations to the surface speed and pressure differential in which non-contacting seals, such as the labyrinth seal, can endure. El-Gamal et al. [11] state that shaft speed has little effect on the leakage performance of straight through labyrinth seals such as a three teeth labyrinth seal. Shaft rotation does affect some types of labyrinth seals and improves the leakage performance of up-the-step seals and has an adverse effect on down-the-step seals [11].

In aero-gas turbines demanding savings in space and efficiency, brush seals can replace labyrinth seals. A well designed and installed brush seal leaks up to 1/10 of the flow in a comparably sized labyrinth seal and will not incite rotordynamic instability [12].

Brush seals consist of a bed of densely packed bristles attached to an outer ring with a backing plate, see Figure 2. The backing plate prevents the bristles from deforming axially under high pressure differentials [5]. The bristles are designed to contact the rotor during operation which prevents air from entering through the dense bristle pack. Persistent contact with the rotor wears the bristles tips and allows for a clearance to develop; and then, the brush seal leakage rate will dramatically increase [13].

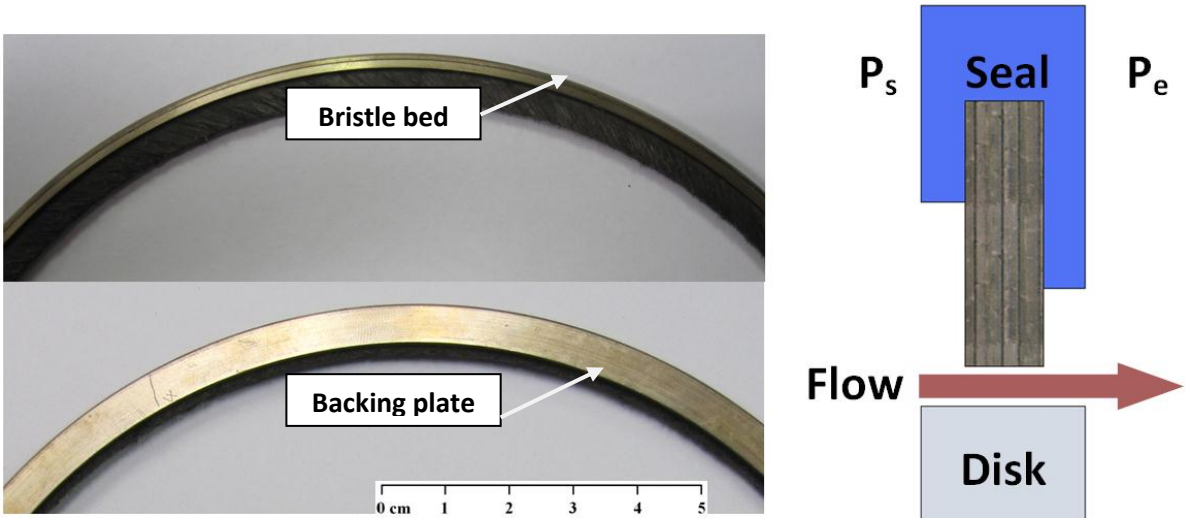

Figure 2. Inner side view of a brush seal and schematic view of air flow.

Note that, because of the high resilience of the bristles, brush seals can withstand large rotor radial excursions without damage. The pressure difference across the seal also induces bristles' blow-down, i.e., a pull-like displacement towards the rotor that closes the clearance and further minimizes leakage. However, the brush seal reduces leakage best when in contact with its rotor [12]. Unfortunately, persistent contact increases drag torque and induces

localized heat generation and severe thermal distortion is not infrequent.

Generally, brush seal bristles are designed to wear its tips while initially in contact with rotor outer surface, i.e., a break-in period. Some design allowances exist to minimize leakage while averting thermal instability of a brush seal due to excessive contact. High temperature operation degrades mechanical properties and bristle tips wear out sooner than under ambient condition operation.

Note that a brush seal can be installed in one direction only, with the bristles in the direction of rotor spinning. Reverse rotor rotation or improper brush seal installation will most likely destroy or permanently deform the seal [1]. Brush seals also have poor axial stiffness since the bristles tend to bend in the direction of the pressure differential. Since the axial bend is dictated by the length the bristles extending beyond the backing support plate, if the bristles are too long and the bending is excessive, the bristle tips may disengage from the rotor and permit a large amount of leakage [13].

Hybrid brush seals (HBS) have evolved to reduce the known disadvantages of brush seals, even allowing for bi-directional shaft rotation, albeit increasing the element mechanical complexity. Hybrid brush seals, as seen in Figure 3, incorporate cantilevered (flexural supports) pads at the end of the bristle matrix in a conventional brush seal. During operation, the cantilever pads generate a hydrodynamic film that lifts the pads whose support elastic elements and bristles have low radial stiffness [14]. Because the pads undergo hydrodynamic lift during operation, the HBS has little heat generation and drag power losses. The gas film prevents any contact between the seal and rotor while permitting a low amount of leakage.

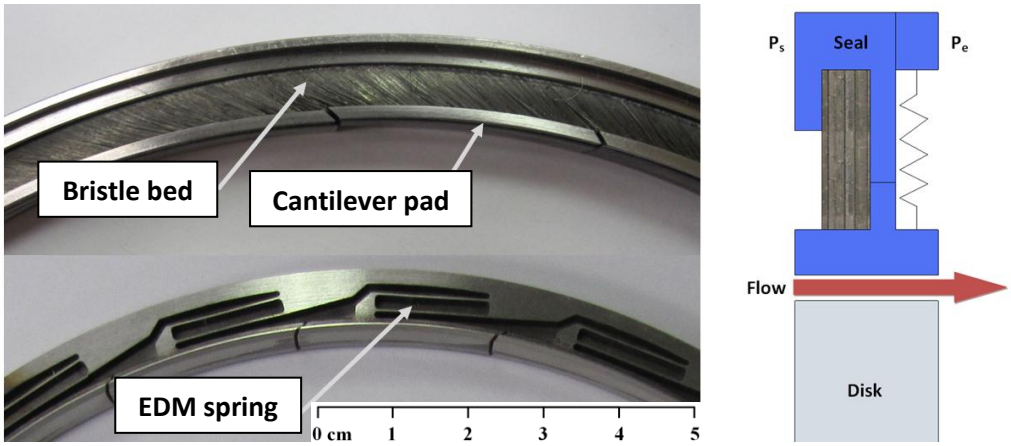

Figure 3. Inner side view of a hybrid brush seal and schematic view of air flow.

One HBS demonstrates reduced gas leakage by 36% than a 1st generation shoed brush seal [15]. The HBS design calls for a larger axial stiffness which enables the seal to operate at higher pressure differentials [15]. Note, however, the HBS has a larger drag torque under unpressurized conditions such as those during machine start-up and shut-down, since the air film is lost and contact ensues with the rotor. The HBS can be slightly off center during assembly since each cantilever pad will lift-off once rotation begins [10].

The Hydrostatic Advanced Low Leakage (HALO^{TM}) seal is a seal type evolving from the HBS. This novel seal is an all-metal compliant seal designed with self-controlling clearance as the pressure differential increases [16]. Of significant note, the novel seal excludes the bristle matrix that is characteristic of a brush seal thus providing a considerably higher axial stiffness. The all-metal compliant seal consists of cantilevered pads positioned at the inlet of the flow, not at the exit as with prior versions of the HBS. A downstream back wall averts the flow from exceeding beyond the cantilevered pad and, instead, the gas flows in the gap between the rotor and the pads' inner surface.

The novel seal is made of steel and assembled with an initial clearance with the rotor. The HBS has its pads with a small converging taper along the axial direction whereas the pads in the all-metal seal have three slanted grooves at various axial planes before leading to a convergence, as seen in Figure 4. Furthermore, the novel seal has a leading (upstream) edge lip intended to draw the pad closer to the disk surface when the seal experiences a pressure differential.

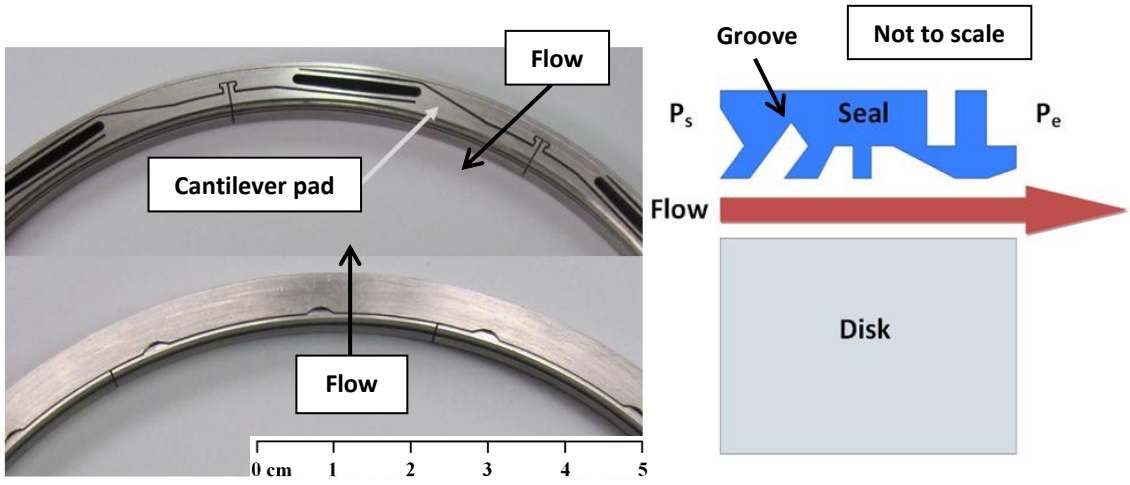

Figure 4. Inner side view of an all-metal seal and schematic view of air flow.

In proprietary tests conducted by San Andrés and Ashton [16], the all-metal seal reveals the lowest flow factor, an estimated 1/3 that of a similar size HBS and an order of magnitude lower than that for a three teeth labyrinth seal. The tests for the novel seal were performed without shaft rotation for increasing supply pressures up to 5 bar and at temperatures up to 300°C. The data confirms the novel seal's excellent sealing features and its potential to revolutionize sealing technology in gas and steam turbines.

Refs. [4] and [17] detail the experimental results from previous work with one labyrinth seal, one conventional brush seal, and one hybrid brush seal (HBS). These results show the HBS overall leakage is 38% less than the brush seal and 61% less than a similarly sized aluminum labyrinth seal.

To continue the progress of this innovative seal technology, the all-metal seal leakage, drag torque and wear rate must be quantified for operating temperatures, pressure differentials, and rotor speeds representative of gas and steam turbines. These test results will evidence the suitability of the novel seal to reduce leakage (secondary flows) in high performance turbomachinery.

CHAPTER III

DESCRIPTION OF HIGH TEMPERATURE GAS SEAL TEST RIG

Figure 5 shows a cross section view of the high temperature seal test rig. Two tapered rolling element bearings (1) support an overhung long and thin shaft (2) and disk (3) inside a pressurization vessel (4) supplied with hot air (5). The tapered geometry of the roller bearings can sustain high axial loads experienced due to the large pressure differentials. The rotor is connected to a direct current (DC) motor (6) (90 V, 9.4 A) through a quill shaft (7) and flexible coupling (8).

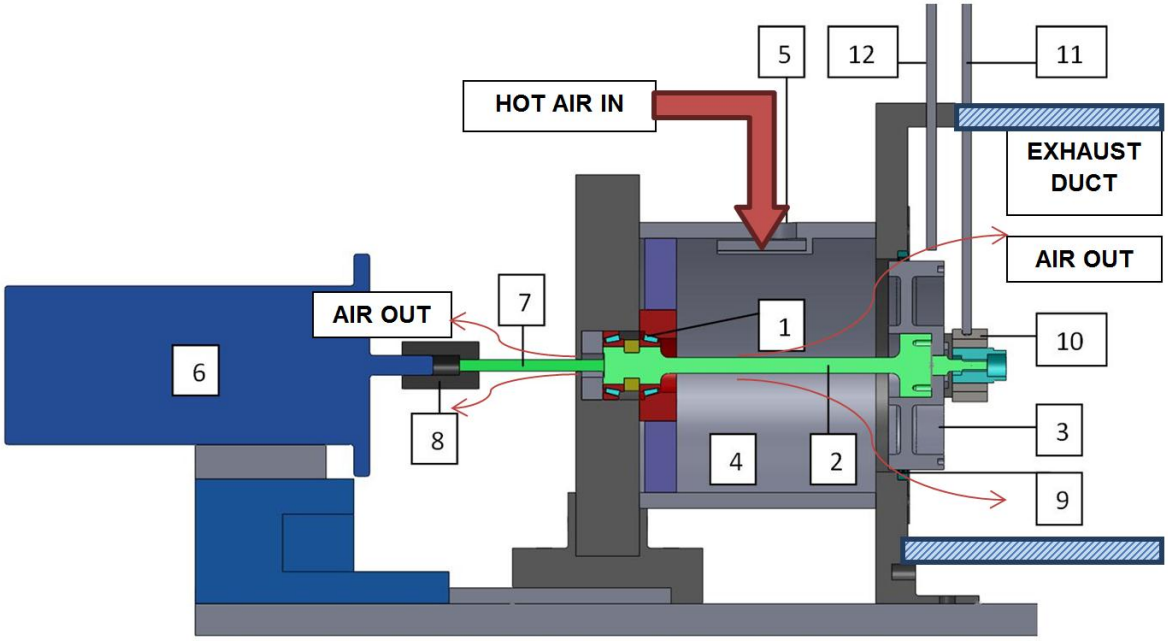

1	Tapered roller bearings	7	Quill shaft
2	Shaft	8	Flexible coupling
3	Disk	9	Test seal
4	Pressure vessel	10	Metal mesh foil bearing (MMFB)
5	Air inlet	11	Position rods
6	Motor	12	Eddy current sensors (X and Y direction)

Figure 5. Cross sectional side view of the high temperature test rig.

A test seal (9) fits in a circumferential groove machined at one end of the vessel and is secured by a thin metal circular gasket and fastening bolts with washers. The cantilever shaft-

disk arrangement permits the simple exchange of test seals without affecting the installation of major components of the system.

A metal mesh foil bearing (10) (MMFB) and rods assembly (11), as shown in Figures 5 and 6, immediately outside of the disk rotor in the exhaust duct, support the free end of the shaft-disk assembly at a concentric position with the test seal.

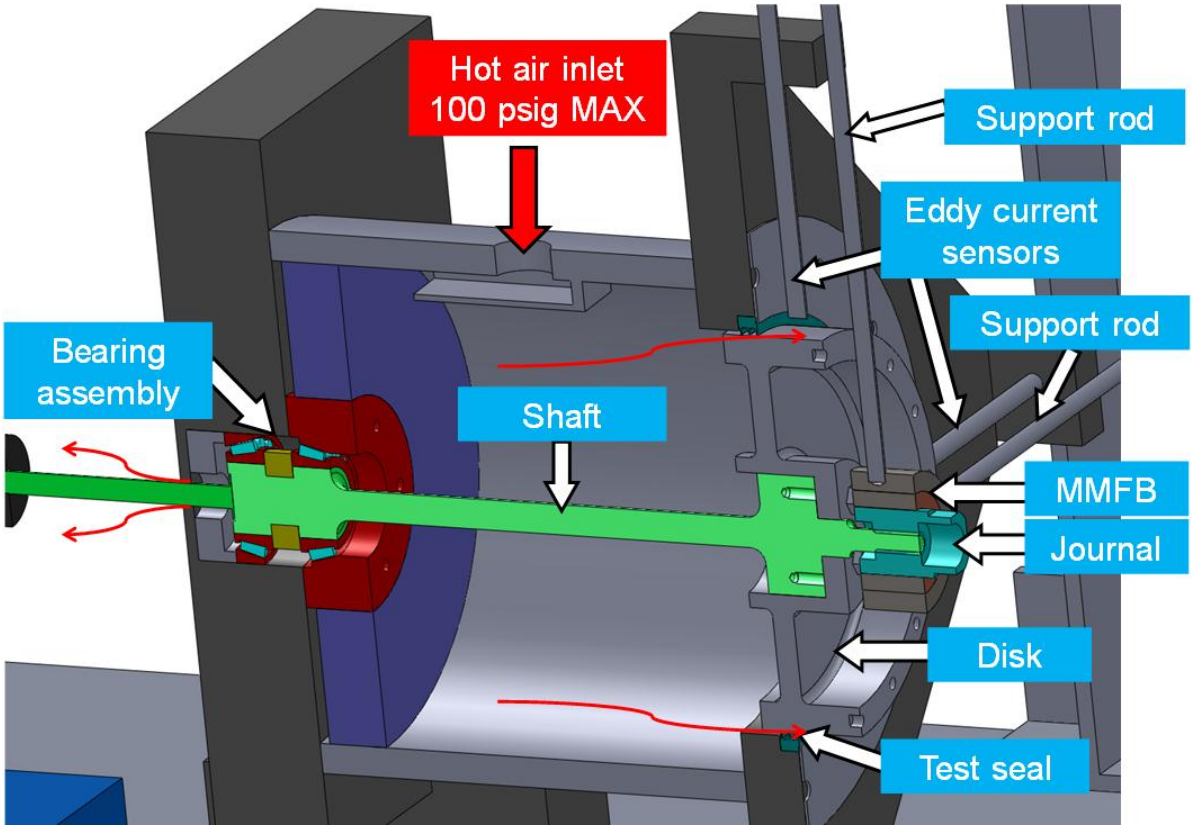

Figure 6. Cross sectional side view of the high temperature test rig.

Figure 7 shows a photograph of the MMFB supporting the free end of the rotor. The MMFB provides both structural stiffness and material damping. A journal, with a polished surface, is mounted on the free end of the shaft to obtain a tight fit with the top foil of the MMFB.

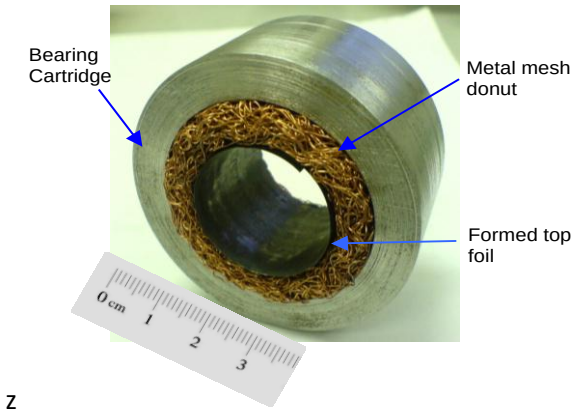

Figure 7. Photograph of metal mesh foil bearing [18].

A thin coating of MoS_2 on the top foil of the MMFB serves to reduce friction at rotor startup and shutdown when the journal contacts the top foil. The top foil contains two flaps in one end which are secured into precise holes in the metal mesh. This feature holds the top foil in place and dictates the direction of rotation. It is important to note that the rotor must spin in the proper direction to protect the top foil from damage [19].

Vertical and horizontal threaded steel rods, attached to an external rigid steel frame, support the MMFB. By tightening/loosening nuts on the rods at the frame location, the MMFB is displaced thereby allowing centering of the disk with respect to the seal. Two eddy current sensors, orthogonally positioned, measure the displacements of the disk in the vertical and horizontal directions.

The eddy current sensors (12) (ECS) are used to locate the disk center when the seal is installed. The radial clearance of the seal is verified visually and with shims to ensure an even gap around the disk before testing. Figure 8 shows the disk positioned concentrically with respect to the seal. The ECS readings are continuously monitored to ensure the center is not displaced during pressurization.

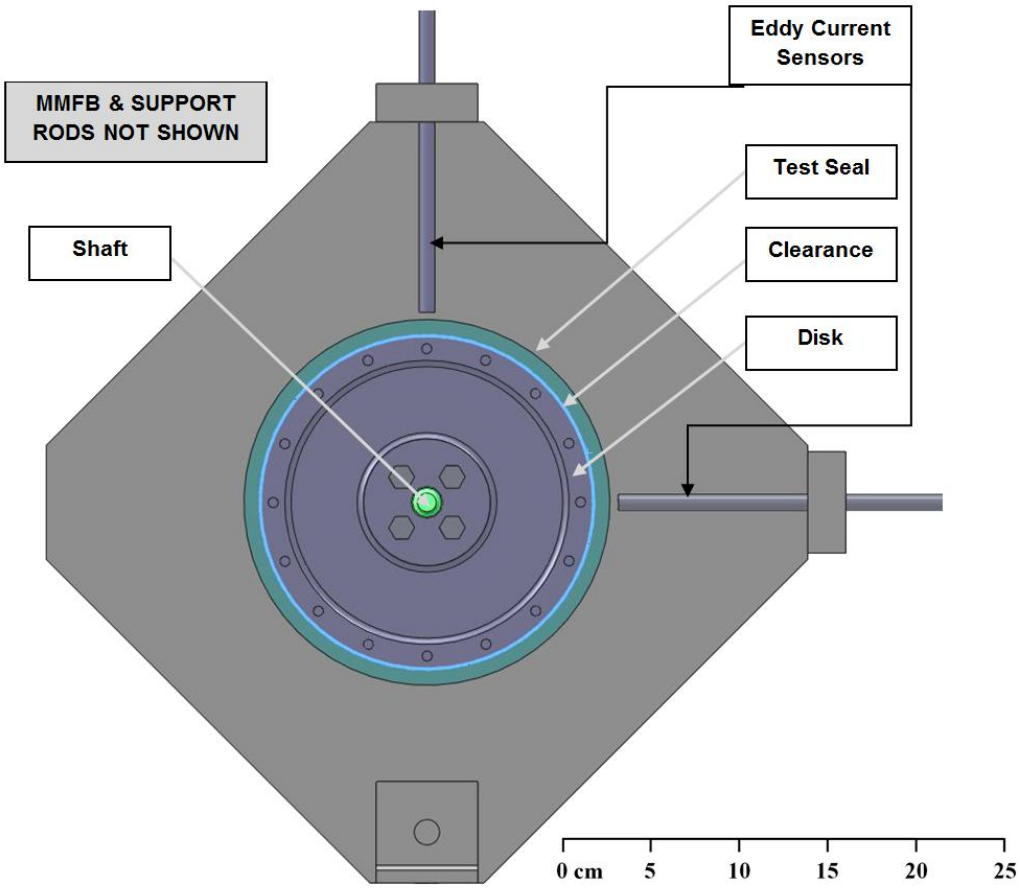

Figure 8. Front view of the test rig depicting the disk positioned concentrically with a seal.

As shown in Figure 9, the rotor support bearings are rolling element tapered bearings that withstand high temperatures when packed with Krytox®, a perfluoropolyether (PFPE) based grease. The bearings' outer races fit into a cylindrical casing in the pressure vessel while the inner races are press fitted onto the shaft end. The bearings are installed with their tapered rolling elements in opposing directions to tolerate the large axial thrust loads generated by the air pressure on the inner side of the disk. For example, a 690 kPa (100 psig) differential pressure will result in an axial load (F) of approximately 15.1 kN (3,400 lb_f).

Also shown in Figure 9, there is an aluminum silicate plate, 25.4 mm (1 in) thickness, which faces the closed end of the pressure vessel and acts as an insulation element that prevents excessive heating of the bearings.

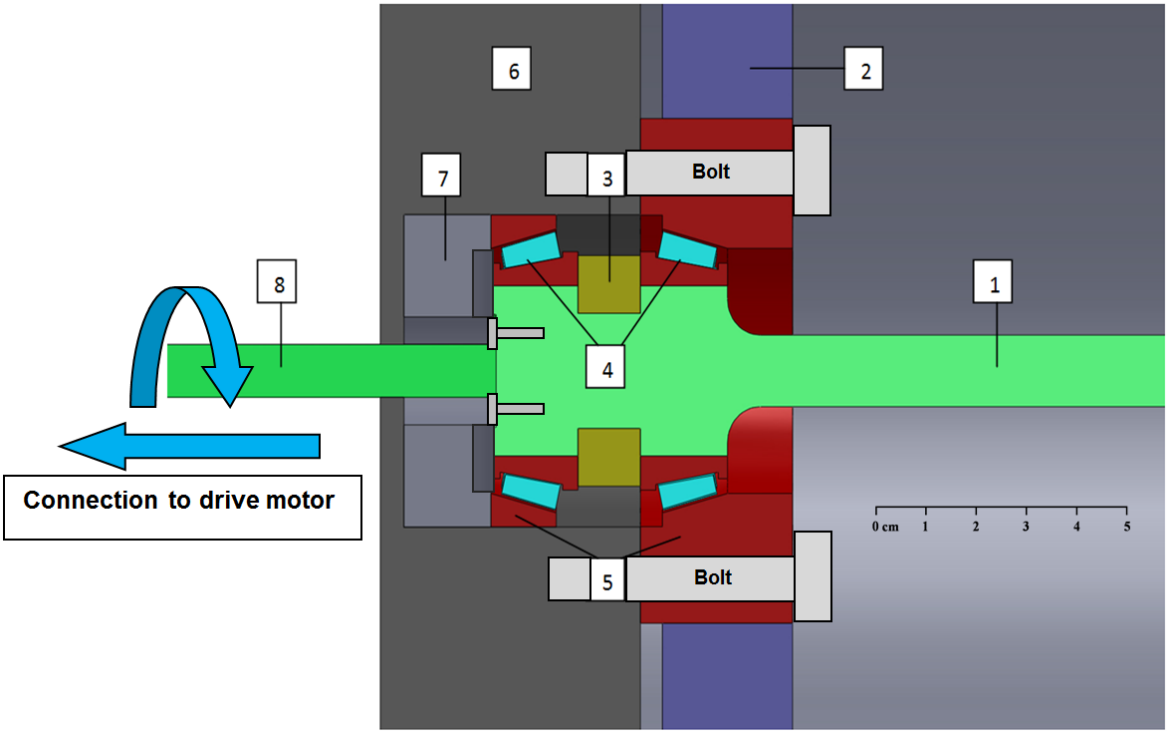

1	Main shaft	5	Bearing races (2)
2	Lava plate	6	Vessel wall
3	Spacer	7	Threaded ring
4	Bearings (2)	8	Quill shaft

Figure 9. Cross section side view of the tapered roller bearings sustaining the rotor.

The test rig is ready for operation upon installation of a seal facing the outer diameter of the disk. Pressurized cold air flows through a particle and coalescing filter to extract impurities, such as water and oil, to prevent damage from particulates to upstream components. The air stream proceeds through a turbine flow meter recording its volumetric flow rate (maximum range ~ 21 ACFM). The gas flows through a turbine and an electrical pulse is generated and converted to a frequency output proportional to the volumetric flow rate. The mass flow rate is determined from the volumetric flow rate for a specific pressure and air temperature at standard air conditions.

Next, cold air flows through an electromechanical control valve into an electric heater (12 kW, 240 V). The electromechanical control valve controls the air flow and upstream pressure. The valve opens gradually, through 14 distinct set positions, until fully opened. The

electric heater warms oil-free incoming air to a set temperature (maximum 300°C) with delivery at a maximum pressure of 8 bar[1]. The air inlet temperature and pressure upstream of a test seal, the rotor speed, and the disk centering are independently controlled throughout the experimental procedure.

The hot air flows into the pressurization vessel where the air inlet temperature and pressure are recorded. A thick layer of thermal insulation covers the test rig entirely and an insulated exhaust duct routes the discharged hot air at ambient pressure through a tall chimney for venting outside the laboratory.

A PC Field Programmable Gate Array (FPGA) sets and controls the electromechanical opening valve, the electrical heater, and the data acquisition. The operator sets the desired air temperature and pressure in the vessel upstream of the seal with a dedicated NI LabVIEW® Virtual Instrument (VI) [17]. The VI records and stores the collected data (pressures, temperatures and flow) for post-processing.

A digital signal analyzer and accelerometer record the natural frequencies of the rotor-bearing system. Mode shapes, depictions of rotor deflection, are constructed using the vibration frequencies created with an impact to the rotor.

XLTRC[2], a rotordynamic software suite, is used to predict the natural frequencies and mode shapes of the rotor. Figure 10 shows the cross section of the rotor modeled. The rotor is supported by two roller element bearings on the motor side and with a metal mesh bearing on the free end. The roller element bearings provide high stiffness and the metal mesh bearing provides a source of stiffness and damping.

[1] The all-metal seal can be operated to a larger pressure differential than the labyrinth seal since its clearance contracts with pressurization.

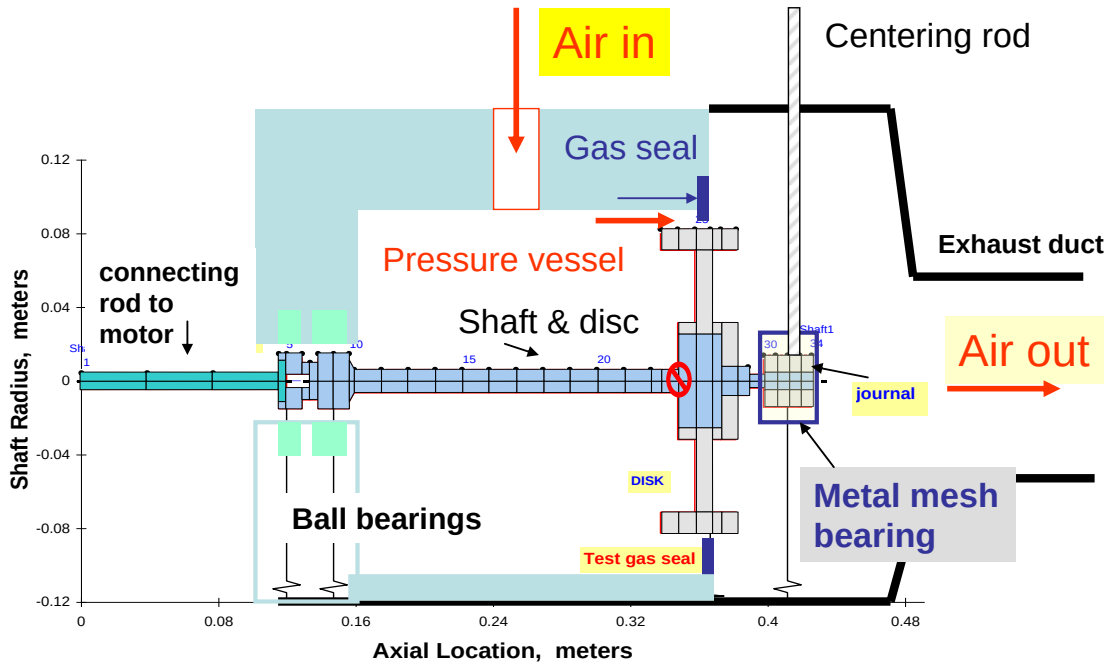

Figure 10. Structural model of the rotor and support bearings.

The natural frequencies are measured and compared to predicted values. The first, second, and third free-free vibration mode shapes of the shaft and disk system are found experimentally and analytically. The free-free mode shapes help predict the behavior of the system during operation. The results are important to avoid contact of components during maximum deflection since a seal clearance is typically small.

CHAPTER IV

DESCRIPTION OF THE TEST SEALS

Table 1 lists the dimensions and materials of the three teeth labyrinth seal and disk pair. Figure 11 shows the layout of the labyrinth seal which makes a diametral clearance of 0.51 mm (0.02 in) with the disk when installed at ambient temperature. This clearance equals the difference between the seal inner diameter, measured with a caliper, and the disk outer diameter, measured with a micrometer. Separate measurements using shims to fill the diametral gap lend credence to the measurements with a caliper and a micrometer.

Table 1. Disk and labyrinth seal geometry and material properties.

Disk Material	4140 Steel
Linear Coefficient of Thermal Expansion, α	11.2 10^{-6}/°C
Outer Diameter, D	166.85 mm
Disk Thickness	44.45 mm
Labyrinth Seal Material	4140 Steel
Linear Coefficient of Thermal Expansion, α	11.2 10^{-6}/°C
Outer Diameter, S_{OD}	183.11 mm
Inner Diameter, S_{ID}	167.36 mm
Seal Axial Length, l	8.40 mm
Number of Teeth	3
Teeth Tip Width	0.17 mm
Number of Cavities	2
Cavity Depth	3.0 mm
Diametral Clearance (C_d=S_{ID}-D)	0.51 mm
Uncertainty in Lengths	± 0.01 mm

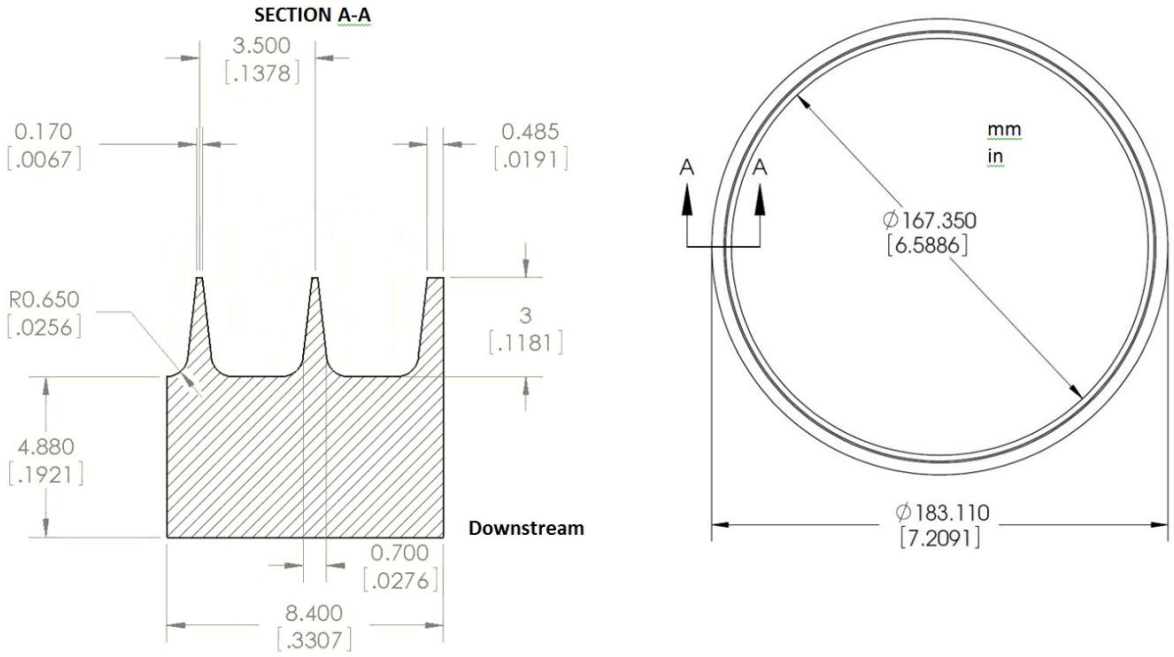

Figure 11. Cross sectional view of steel three teeth labyrinth seal. Dimensions in mm [in].

The all-metal seal is a sealing type that supersedes the hybrid brush seal (HBS). Table 2 lists the seal geometry and material properties. The diametrical clearance with the disk at ambient conditions is 0.43 mm.

Table 2. All-metal seal geometry and material properties.

Material	Inconel 718
Linear Coefficient of Thermal Expansion, α	12.0 10^{-6}/°C
Outer Diameter, S_{OD}	183.05 mm
Inner Diameter, S_{ID} (Upstream)	167.28 mm
Inner Diameter, (Downstream)	167.10 mm
Seal Axial Length	8.48 mm
Pad Allowable Radial Movement	0.27 mm
Pad Axial Length, l	8.05 mm
Pad Arc Length (40°)	58.42 mm
Number of Pads	9
Beam Axial Width	6.40 mm
Diametral Clearance (C_d=S_{ID}-D)	0.43 mm
Uncertainty in Lengths	± 0.01 mm

The novel seal, shown in Figure 12, is an all-metal component manufactured with an electrical discharge machining (EDM) process. The seal comprises of nine arcuate pads cantilevered from an outer rim. The compliance of the thin beams (flexures) facilitates radial displacement of the pads. A downstream plate blocks any flow through the gaps behind the pads. The pads are not flat, but have a machined axial profile that promotes the development of hydrostatic pressure to lift-off the pads with rotor speed thus ensuring non-contact operation [16].

Some of the prominent features and benefits of the non-contacting seal are that it allows shaft counter-rotation and is readily installed with an initial nominal clearance. The all-metal seal is ideally suited for industrial gas turbines and large steam turbines.

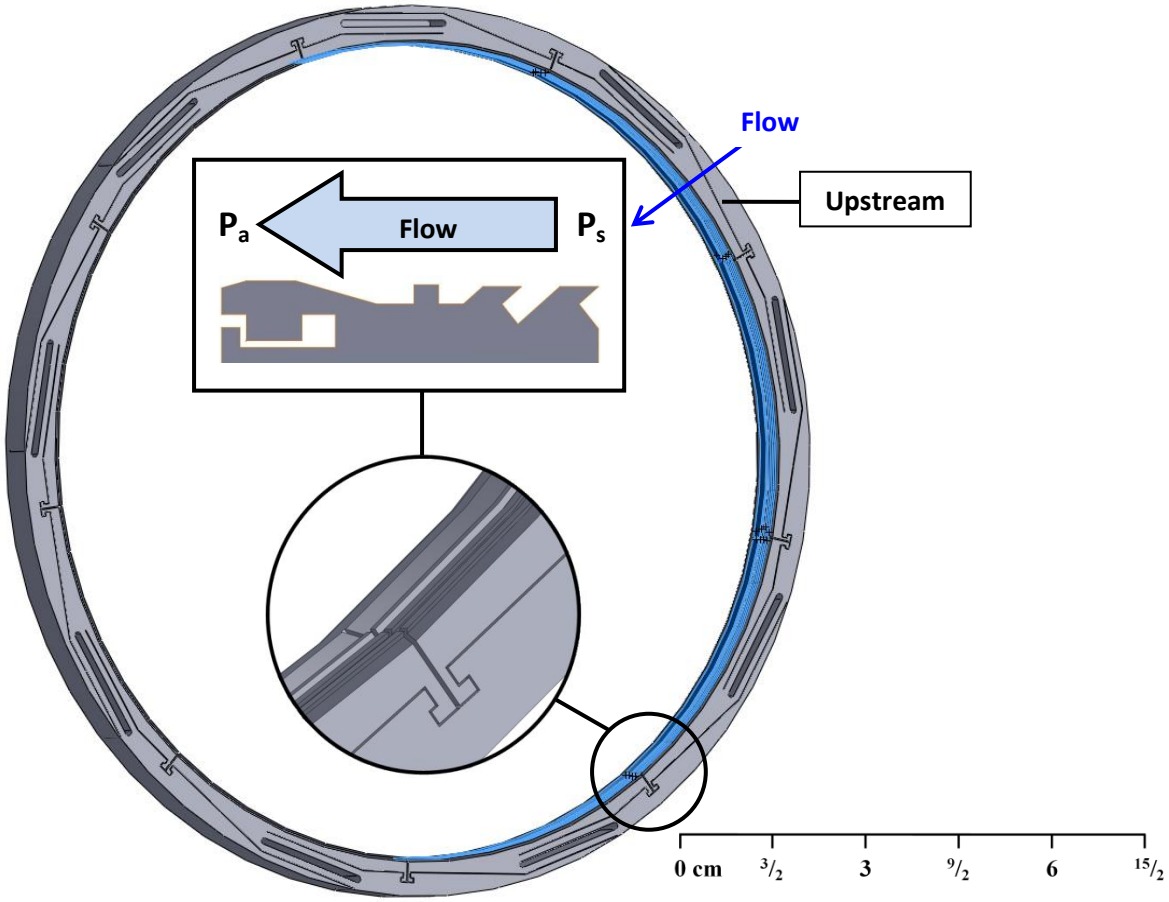

Figure 12. The all-metal seal with inset showing its axial profile.

Upon installation in the test rig, the all-metal seal assembled diametral clearance equals 0.43 mm (0.017 inch). Note that the seal pads can displace radially a maximum of 0.27 mm (the gap between spring elements). This is a clearance-controlled seal; i.e., with external pressurization, the flexures shift the pads towards the disk thus closing the gap [16].

Note that the design seeks to operate the seal (always) with a pressure drop to produce a sufficiently small gap (clearance) [3]. The axial profile feature works well with high supply pressures which pushes the seal pads to displace towards the rotor [3].

Recall that at ambient conditions, the labyrinth seal has a diametral clearance of ~ 0.51 mm, similar in size to that of the all-metal seal whose diametral clearance is ~ 0.43 mm.

CHAPTER V

LEAKAGE MEASUREMENTS WITH A LABYRINTH SEAL – NO ROTOR SPINNING

The leakage (g/s) exiting the flow area, *A*, between the labyrinth seal inner diameter and disk outer diameter is measured for increasing air inlet temperatures (30°C, 100°C, 200°C and 300°C). The measurements were conducted without the rotor spinning and with air conditions as listed in Table 3.

Table 3. Air inlet and exhaust conditions for labyrinth seal leakage measurements.

Specific Gas Constant	287 J/kg-K
Supply Pressure, P_s	101 kPa - 505 kPa
Inlet Temperature, T_s	303°K - 573°K
Exhaust Pressure, P_a	101 kPa
Ambient Temperature, T_a	303°K

A control valve is opened from a fully closed position to increase the supply pressure (P_s) into the test seal. The seal mass leakage $(\dot{m})$ typically increases with an increasing pressure drop, while it decreases with increasing gas temperature due to the decrease in air density (ρ). The ratio of supply pressure (P_s) to the exhaust pressure (P_a) is defined as a pressure ratio

$$p_r = \frac{P_s}{P_a} \tag{1}$$

The gas flow reaches a choked condition when the gas velocity reaches sound speed. The gas ratio of specific heats, γ, determines the pressure ratio ($p_{r,\,choke}$) when the air flow begins to choke (assuming gas behavior is ideal), i.e.,

$$p_{r,choke} = \left(\frac{\gamma+1}{2}\right)^{\gamma/(\gamma-1)} = \frac{P_s}{P_a} \tag{2}$$

The mass flow rate after the gas becomes choked increases linearly with increasing supply pressure. The specific heat ratio of air is γ~1.40 at 30°C and determines that the flow becomes choked above a pressure ratio of 1.89. γ~1.38 at 300°C and thus p_r=1.88, indicating a slight decrease of p_r with increasing temperature.

Figure 13 depicts the measured leakage for the labyrinth seal versus pressure ratio (P_s/P_a) for increasing temperatures up to 300°C. The labyrinth seal mass flow rate measurements are recorded[2] up to 65 g/s at a pressure ratio of 3.5 and at 30°C which is the maximum flow of the flow meter range. The lowest mass flow rate recorded at a pressure ratio (P_s/P_a) of 3.5 is approximately 45 g/s. The measurements show a 31% (20/65) decrease in leakage from an ambient air temperature to an air temperature of 300°C at a pressure ratio of 3.5, for example.

Table 4 lists the uncertainties in leakage and pressure ratio. In the figure, error bars with the data points show the uncertainty at a 95% confidence interval. The leakage measurements taken without rotor speed do not include an uncertainty for the gas temperature.

Table 4. Uncertainties for mass flow rate and pressure ratio for measurements with a labyrinth seal.

	Average %	Maximum %
Mass Flow Rate	0.6	3.7
Pressure Ratio	0.8	2.8

[2] All tests conducted with the rear end of the test rig (shaft stub and coupling) closed.

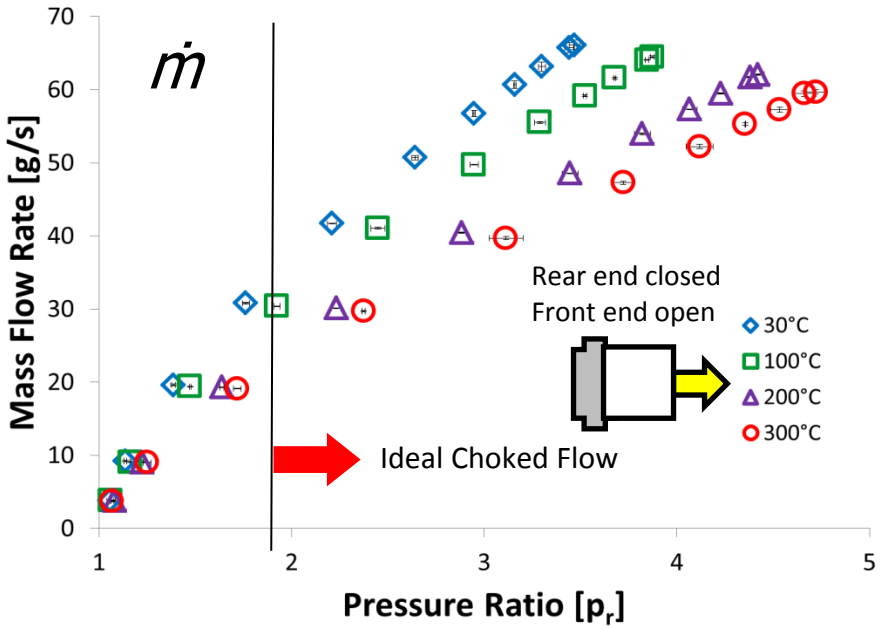

Figure 13. Labyrinth seal: mass flow rate $\dot{m}$ vs. pressure ratio, $p_r=P_s/P_a$. Non-rotating disk and air at four temperatures (30°C, 100°C, 200°C, and 300°C). Discharge at ambient pressure (P_a).

Delgado and Proctor [6] recommend using a flow factor Φ to compare the leakage performance of different seal types with dissimilar operation characteristics and geometry. The flow factor accounts for the seal size (rotor diameter, D), inlet temperature T_s [K], and supply pressure P_s [Pa].

$$\Phi = \dot{m}\sqrt{T}\Big/_{P_s D} \tag{3}$$

Figure 14 shows the derived flow factor (Φ) for the labyrinth seal versus pressure ratio. Φ reaches a maximum of 20 kg-K$^{0.5}$/(MPa-m-s) and remains constant when the pressure ratio (p_r) is greater than the choke pressure ratio ($p_{r,\,choke}$). The flow factor is proportional to the pressure ratio (p_r) when the pressure ratio is below choke pressure ($p_{r,\,choke}$). Figure 14 shows the flow factor also removes the flow dependency of temperature.

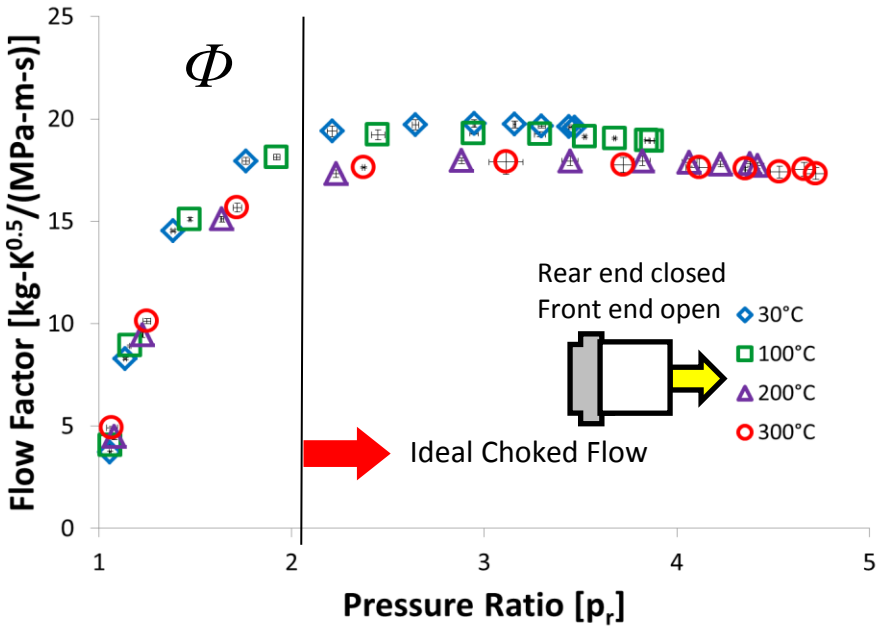

Figure 14. Labyrinth seal: flow factor Φ vs. pressure ratio, $p_r=P_s/P_a$. Non-rotating disk and air at four temperatures (30°C, 100°C, 200°C, and 300°C). Discharge at ambient pressure (P_a).

The data in Figure 14 collapses into a single curve demonstrating the suitable application of the flow factor introduced in Ref [6].The flow factor (Φ) removes the effect of the dissimilar operating conditions, temperature in this case. The variation in the four temperature conditions can be attributed to the decrease in clearance with increasing temperature (thermal expansion). Only the disk outer diameter measured at an ambient condition is used to calculate the flow factor for all temperature conditions.

Appendix D details the derivation and results of the volumetric flow rate, Q, for the labyrinth seal.

CHAPTER VI

CLEARANCE MEASUREMENTS FOR THE LABYRINTH SEAL AND PREDICTIONS OF LEAKAGE

Clearance Model

Figure 15 shows the disk (outer diameter), seal (inner diameter), and housing (inner diameter) expanding outwards as a result of thermal expansion. The seal outer diameter will expand until the gap (in red) is filled. The seal outer diameter will then be restricted and the seal inner diameter will contract towards the disk thereby reducing the clearance. A clearance model is developed to predict the changes in gap the labyrinth seal experiences with increasing temperature. A (long) cylindrical solid increases its diameter ($\Delta\zeta$) due to thermal expansion as

$$\Delta\zeta = \alpha \times \Delta T \times \zeta \tag{4}$$

where α represents the thermal expansion coefficient of the material [/^{o}C], ΔT is the change in temperature [°C], and ζ denotes the outer diameter at a reference (cold) temperature.

Both the outer diameter of the disk (D) and the inner diameter of the seal (S_{ID}) expand with an increase in temperature. Below subscripts *s*, *d*, and *h* designate the seal, disk, and housing, respectively. The outward thermal expansion of the disk causes a reduction in clearance, while the thermal growth of the seal increases the clearance. Ashton [17] reports the clearance as

$$\Delta C_1 = \alpha_s \times \Delta T_s \times S_{ID} - \alpha_d \times \Delta T_d \times D \tag{5}$$

Note that there is a gap of 0.020 mm between the seal outer diameter and its seating in the housing. Hence, there is also thermal expansion of the seal material in this gap. Since the outer diameter of the seal (S_{OD}) expands faster than the inner diameter of the housing (H_{ID}), the housing actually restricts the seal outer diameter expansion at high temperatures. The change in diametral clearance is

$$\Delta C_2 = \alpha_s \times \Delta T_s \times S_{OD} - \alpha_h \times \Delta T_h \times H_{ID} - 0.02mm \tag{6}$$

If ΔC_2 is negative, it means the outer diameter of the seal expands outwards and is not accounted for in the seal clearance change. Otherwise, the outer diameter expands inwards due to the contact with the housing inner diameter and reduces the clearance.

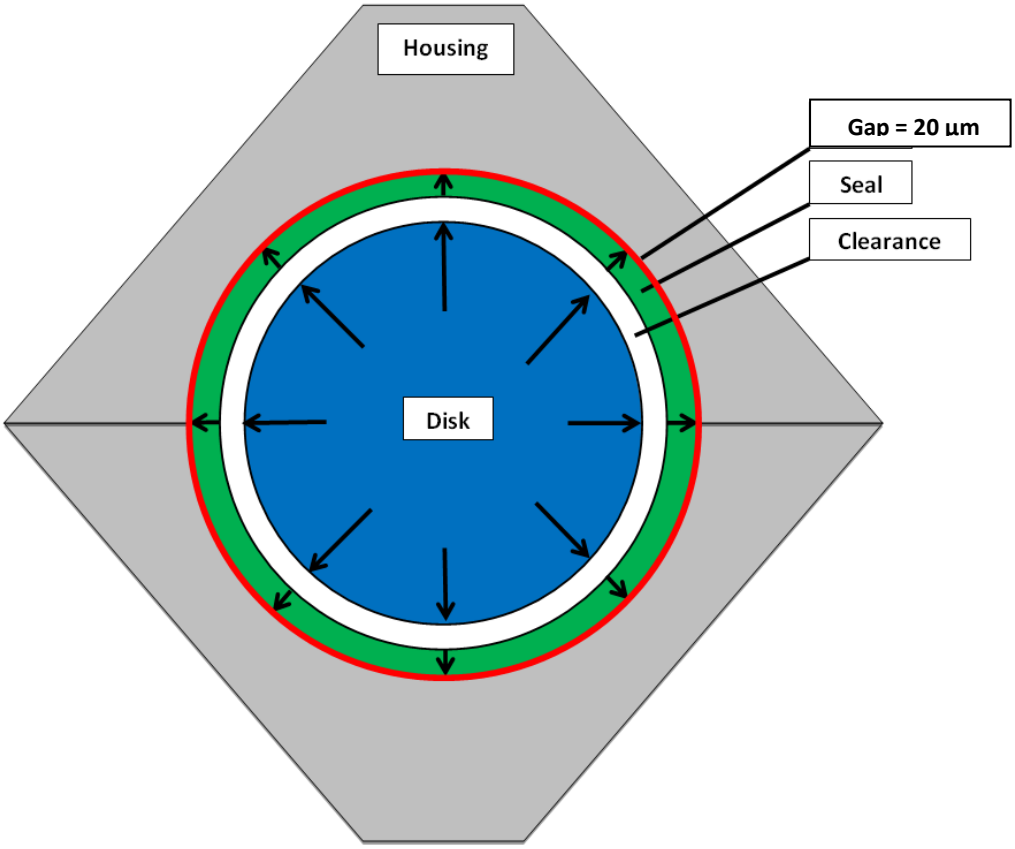

Figure 15. Expansion direction of thermal components.

The total change in clearance, ΔC, once all the thermal expansion effects are accounted for is

$$\Delta C = \Delta C_1 - \Delta C_2 \tag{7}$$

ΔC must be subtracted from the initial clearance at 30°C to obtain the total change in clearance after all the thermal expansion effects are considered. The fully expanded form of the clearance change is

$$\Delta C = [\alpha_s \times \Delta T_s(S_{ID} - S_{OD}) + 0.02mm] - \alpha_d \times \Delta T_d \times D + \alpha_h \times \Delta T_h \times H_{ID} \tag{8}$$

Figure 16 shows the thermocouple locations for the labyrinth seal, disk, and housing temperature used in the model. The thermocouples measuring the components are placed significantly apart and are used to determine the general temperature behavior at steady state conditions.

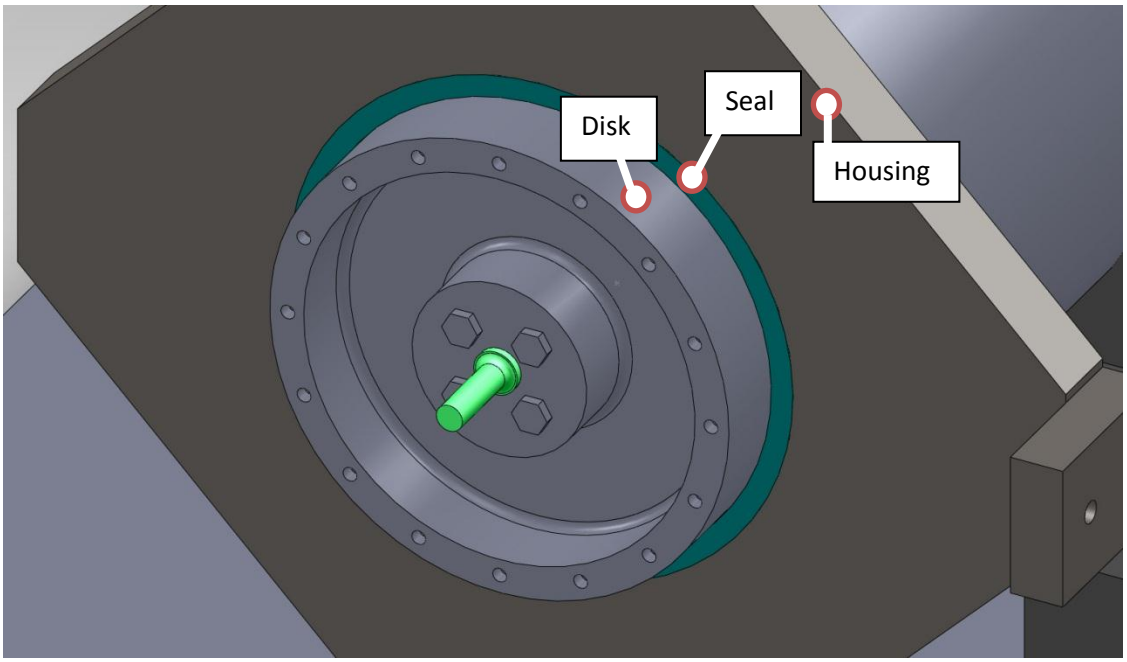

Figure 16. Thermocouple locations for the seal, disk, and housing temperature.

Table 5 shows the dimensions for the labyrinth seal, disk, and housing used in the model. Recall Table 1 for the labyrinth seal and disk dimensions and properties.

Table 5. Component dimensions and material properties.

Component	Labyrinth seal	Disk	Housing
Inner diameter [mm]	S_{ID}=167.36	-	H_{ID}=183.13
Outer diameter [mm]	S_{OD}=183.11	D=166.85	-
Thermal expansion coefficient [/°C]	α_s=1.12 10^{-5}	α_d=1.12 10^{-5}	α_h=1.20 10^{-5}

Figure 17 shows the recorded temperatures of the housing, disk as reported in Ref. [17] for an aluminum labyrinth seal[3]. Recall the current labyrinth seal is made of steel. These temperatures are used to calculate the change in temperature for the housing, current seal, and disk when the air temperature reaches a steady state at 30°C, 100°C, 200°C, and 300°C. The steel labyrinth seal temperature is assumed to increase similarly to the recorded temperature of the aluminum seal.

It is important to note that the steel housing, seal, and disk do not reach the same temperature as the air temperature. This causes an uneven growth of components due to the radial thermal gradient in the system.

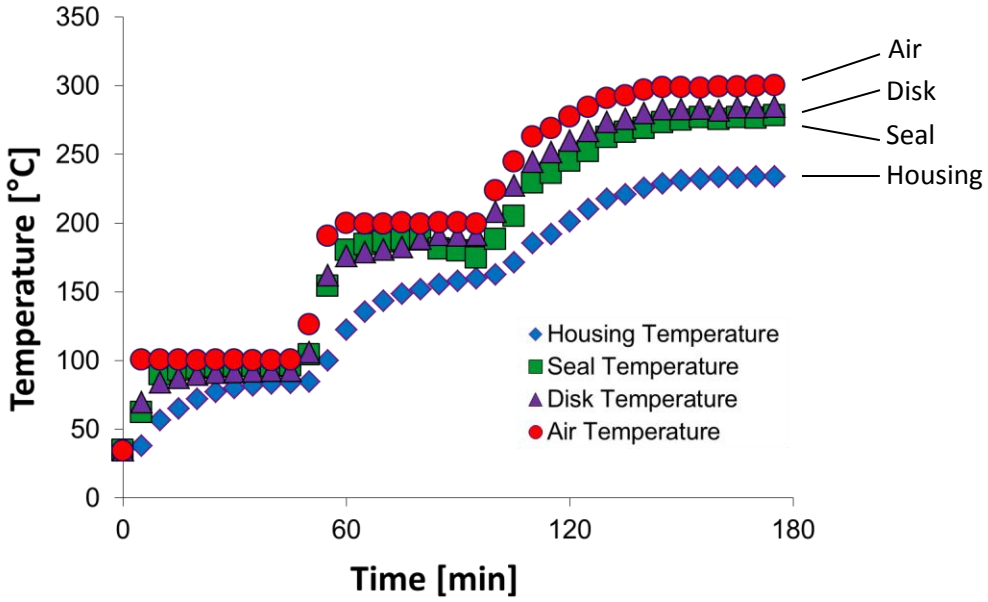

Figure 17. Measured temperature of the labyrinth seal, disk, and housing over time [17].

Table 6 displays the recorded temperatures of the components. The disk and seal are hotter than the housing since the hot air is flowing through the clearance between the seal and disk.

[3] The aluminum labyrinth seal in Ref. [17] has ~ twice the clearance than the (current) steel labyrinth seal

Table 6. Labyrinth seal measured and predicted clearance at increasing temperatures.

Air Temperature	ΔT_h	ΔT_s	ΔT_d	Measured Diametrical Clearance	Total Decrease in gap	Predicted Diametrical Clearance	Total Decrease in gap
30°C	0°C	0°C	0°C	0.508 mm	0 mm	0.508 mm	0 mm
100	45	65	65	0.469 mm	0.039 mm	0.496 mm	0.012 mm
200	120	160	160	0.460 mm	0.048 mm	0.469 mm	0.039 mm
300	195	255	255	0.444 mm	0.064 mm	0.441 mm	0.067 mm
	Ref. [17]						

Measurements of the seal diametral clearance were also obtained using eddy current sensors. Both sensors were calibrated before taking the clearance measurements to determine their sensitivity. Appendix A shows the calibration procedure. The disk is pushed upwards until there is contact with the inner diameter of the seal and the output voltage is recorded. The disk is then pushed downwards until it contacts the seal and the output voltage is recorded. The diametrical clearance is obtained by converting the voltage difference at these two conditions to displacement using the sensitivity for the vertical sensor. The same procedure is repeated in the horizontal direction. The clearance for the vertical direction and horizontal direction is averaged to obtain the measured clearance in Figure 18.

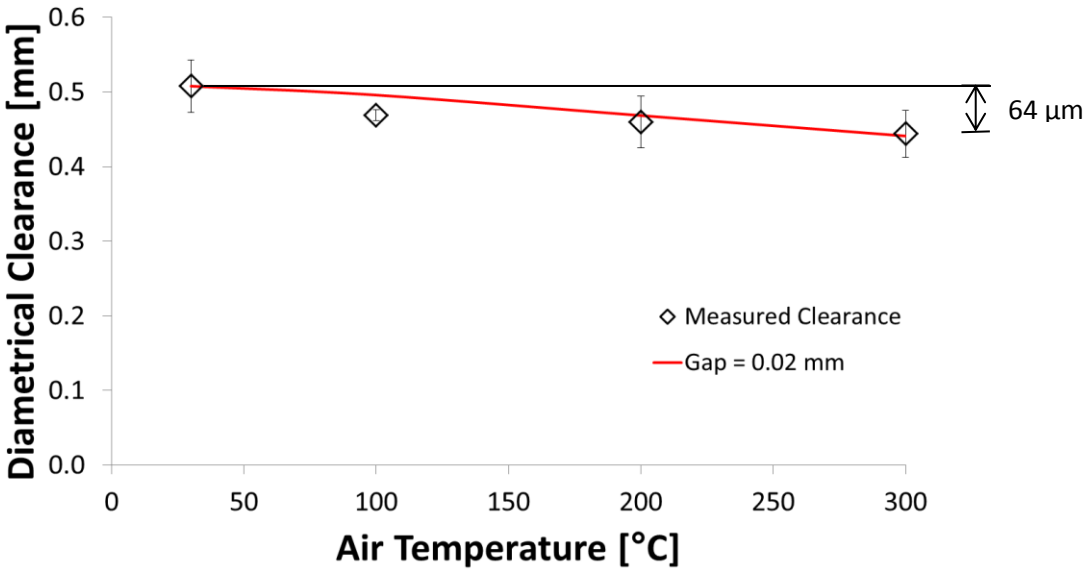

Figure 18. Predicted and measured diametrical clearances vs. temperature for steel labyrinth seal.

Note that the clearance decreases approximately 15% from its initial value over the temperature range of 30°C to 300°C. The measured steel labyrinth diametral clearance decreases from 0.508 mm at 30°C to 0.444 mm at a steady temperature of 300°C.

Leakage Model

Thorat [20] developed XLLaby1CV®, a code for prediction of leakage and force coefficients of gas labyrinth seals with teeth-on-rotor or teeth-on-stator configurations. Thorat's code is used for predicting the leakage trough the labyrinth seal. Table 7 shows the data for the gas and labyrinth seal dimensions with the measured clearances as temperature increases, shown in Table 6, as input to the predictive code. The Neumann leakage model, one of two models available in XLLaby1CV®, is used to predict the seal flow rate. The model accounts for both a flow coefficient and a kinetic energy carryover coefficient.

Table 7. Input data for prediction of leakage in labyrinth seal (radial clearance: 0.254 mm).

Leakage model	Neumann
Seal radius, $½S_{ID}$	83.65 mm
Radial clearance, C_r	0.254 mm
Number of teeth	3
Tooth location	Stator
Tooth height	3 mm
Axial cavity length	2.8 mm
Kinematic viscosity	$3.33\ 10^{-5}$ m^2/s
Reservoir temperature, T_s	303-573°K
Reservoir pressure, P_s	1.5 – 3.5 bar
Sump pressure, P_a	1 bar
Specific heat ratio	1.4
Gas Constant	287 J/(kg$^-$K)
Compressibility factor	1

Figure 19 shows the predicted labyrinth seal leakage versus pressure ratio for increasing supply temperatures. The predictions are derived using the measured radial clearance. The leakage decreases with increasing air temperature and increases with an increasing supply pressure. The predictions are slightly higher for the ambient and 200°C temperature conditions than the measured leakage but are otherwise in good agreement.

The predicted seal leakage decreases with increasing temperature since the flow area decreases. The predicted seal leakage may decrease further with rotor speed operation due to centrifugal growth of the disk at high rotational speeds [3].

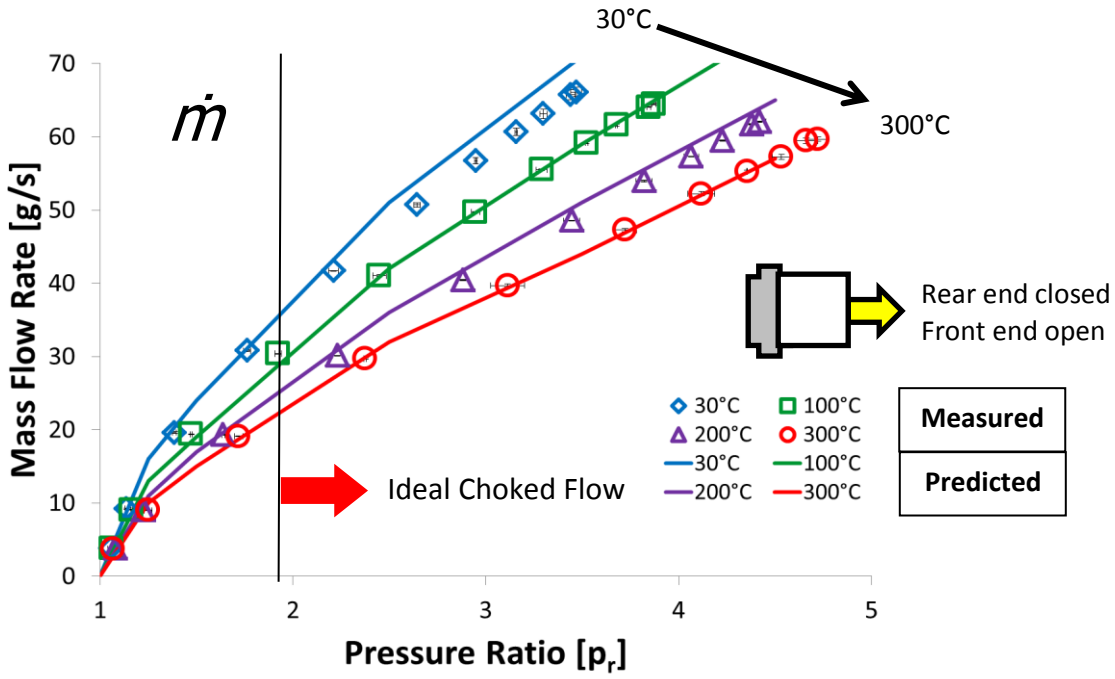

Figure 19. Labyrinth seal: Measured and predicted leakage $\dot{m}$ vs. pressure ratio, $p_r=P_s/P_a$. Non-rotating disk and air at four temperatures (30°C, 100°C, 200°C, and 300°C).

Figure 20 shows the predicted and test flow factors for the labyrinth seal. The predicted flow factor for the labyrinth seal remains constant when the pressure ratio is greater than the choke pressure ratio. The flow factor corresponds well with the measured magnitudes and follows the same behavior previously described.

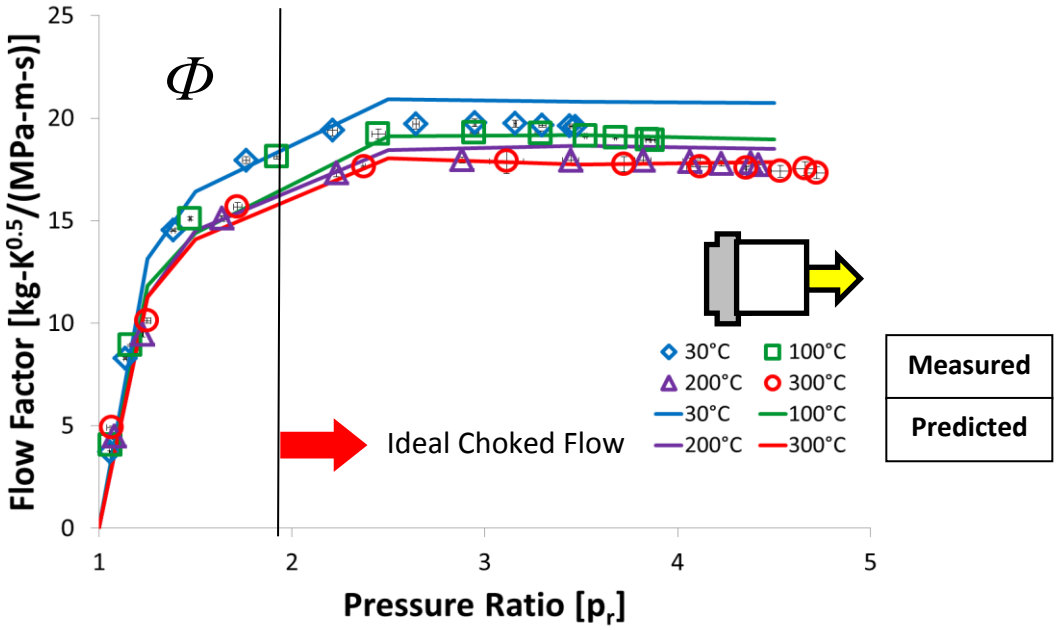

Figure 20. Labyrinth seal: Measured and predicted flow factor Φ vs. pressure ratio, $p_r=P_s/P_a$. Non-rotating disk and air at four temperatures (30°C, 100°C, 200°C, and 300°C).

CHAPTER VII

LEAKAGE MEASUREMENTS WITH AN ALL-METAL SEAL – NO ROTOR SPINNING

The leakage (g/s) exiting the clearance between the novel seal inner diameter and disk outer diameter was measured for increasing air inlet temperatures (30°C, 100°C, 200°C and 300°C). The measurements were conducted without the rotor spinning and with air conditions as listed in Table 8.

Table 8. Air inlet and exhaust conditions for all-metal seal leakage measurements.

Specific Gas Constant	287 J/kg-K
Supply Pressure, P_s	101 kPa - 707 kPa
Inlet Temperature, T_s	303°K - 573°K
Exhaust Pressure, P_a	101 kPa
Ambient Temperature, T_a	303°K

Leakage measurements with the all-metal seal were obtained following a similar procedure as that with the labyrinth seal. A control valve, opened from a closed position, delivers flow at a supply pressure (P_s) into the test seal. The metal compliant seal reduces its operating clearance as the pressure increases and hence decreases the mass flow rate. The lower leakage allows the flow meter to record measurements at higher pressure differentials. The seal mass leakage typically increases with increases in supply pressure, while it decreases with increasing gas temperature due to the decrease in air density and an increase in viscosity.

Figure 21 depicts the measured leakage for both the labyrinth seal and the all-metal compliant seal for increasing temperatures up to 300°C. The metal seal leaks 50% or less than the labyrinth seal. For (P_s/P_a) > 3.5, the all-metal seal flow rate is ~ 15% of the leakage with the labyrinth seal. The novel seal does demonstrate excellent sealing characteristics. Moreover, tests with the novel seal proceeded to higher pressure ratios (max. $P_s/P_{a=}7$), a feature that could not be achieved with the labyrinth seal, since its leakage quickly reached

the maximum range of the flow meter. In the figures, error bars with the data points depict uncertainties at a 95% confidence interval. Table 9 lists the average and maximum uncertainties in leakage and pressure ratio for the all-metal seal leakage measurements.

Table 9. Uncertainties for mass flow rate and pressure ratio for measurements with all-metal seal.

	Average %	Maximum %
Mass Flow Rate	0.9	5.3
Pressure Ratio	1.9	15.1

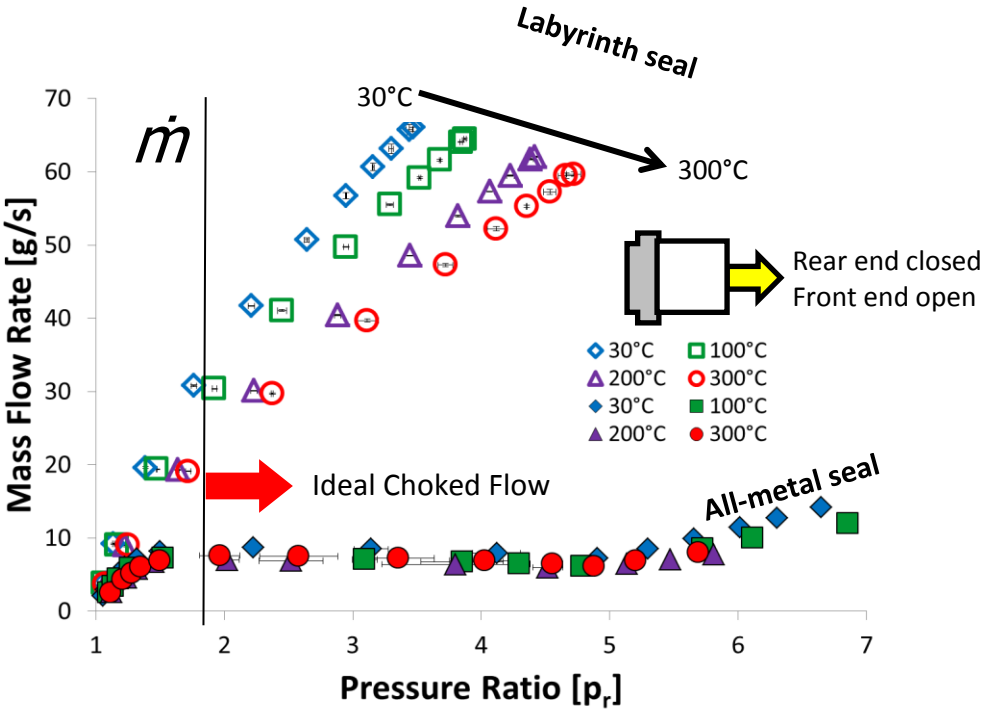

Figure 21. All-metal seal and labyrinth seal: mass flow rate $\dot{m}$ vs. pressure ratio, $p_r=P_s/P_a$. Non-rotating disk and air at four temperatures (30°C, 100°C, 200°C, and 300°C). Discharge at ambient pressure (P_a).

The mass flow rate for the novel seal remains constant for P_s/P_a=2 to 5. The pads in the seal, flexibly mounted, are drawn towards the rotor as the upstream (supply) pressure increases. Then, the pads reach their maximum displacement and the leakage begins to increase with further increases in pressure supply. At P_s/P_a=2, the all-metal seal produces

~25% of the leakage in the labyrinth seal at ambient temperature, and ~30% at 300°C. At P_s/P_a=3.5, the all-metal seal produces ~13% of the leakage in the labyrinth seal at ambient temperature and ~17% at 300°C.

Figure 22 shows the flow factor (Φ) versus pressure ratio for both seals and for increasing temperatures to 300°C. Φ for the novel seal approaches 2 kg-K$^{0.5}$/(MPa-m-s) and remains constant when P_s/P_a > ~ 3.5. At P_s/P_a=2, the all-metal seal flow factor is ~30% of the flow factor obtained with the labyrinth seal. At P_s/P_a=3.5, Φ for the all-metal seal is about 15% of the flow factor for the labyrinth seal. Note Φ for both seals is proportional to the pressure ratio, $p_r < p_{r,\ choke}$. The flow factor characterizes well the leakage for both seals (i.e., the effect of temperature is removed).

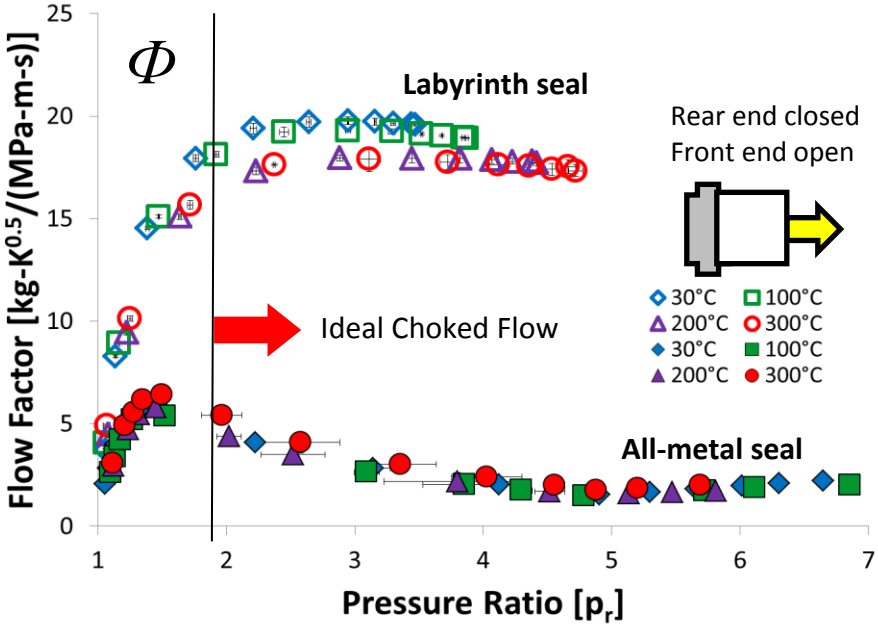

Figure 22. All-metal seal and labyrinth seal: flow factor Φ vs. pressure ratio, $p_r=P_s/P_a$. Non-rotating disk and air at four temperatures (30°C, 100°C, 200°C, and 300°C). Discharge at ambient pressure (P_a).

CHAPTER VIII

LEAKAGE MEASUREMENTS FOR THE LABYRINTH SEAL AND ALL-METAL SEAL OPERATING WITH ROTOR SPEED

This chapter presents the leakage measured with both the labyrinth seal and the all-metal seal for increasing air inlet temperatures (30°C, 100°C, 200°C and 300°C). The measurements were conducted with the shaft rotating at 1000 rpm, 2000 rpm, and 2700[4] rpm. For the novel seal, the tests were conducted at much lower pressure supply conditions than those reported in the previous chapter. The disk expands and reduces the clearance as both the shaft speed and temperature increase. It is important to quantify the effects that rotor speed and operating temperature have on the seals' leakage. Industry continues to push the limits of turbomachinery as higher temperatures increase efficiency and higher rotational speeds increase power output.

The leakage exiting the through the rear of the test rig is quantified first by sealing the front of the test rig with a cap. This parasitic leakage occurs at the location where the rotor shaft exits and connects to the drive motor. The electromechanical valve is opened until a pressure ratio of ~8 is reached.

Figure 23 depicts the measured leakage through the rear side of the test rig versus increasing pressures. The measurements are taken for increasing air inlet temperatures (30°C, 100°C, 200°C and 300°C) similar to those with the test seals. Presently, this parasitic leakage will be subtracted from the flow rate measurements gathered at the conditions with rotor speed and with the seals installed in the test rig.

Table 10 lists the uncertainty in flow and pressure for the rear end leakage measurements. The leakage measurements taken with rotor speed do not include uncertainty for temperature or rotor speed.

[4] With a disk diameter of 166.9 mm, the disk outer diameter surface speed equals 23.6 m/s at a rotational speed of 2700 rpm.

Table 10. Uncertainties for mass flow rate and pressure ratio for leakage thru rear end.

	Average %	Maximum %
Mass Flow Rate	0.3	2.8
Pressure Ratio	0.6	3.2

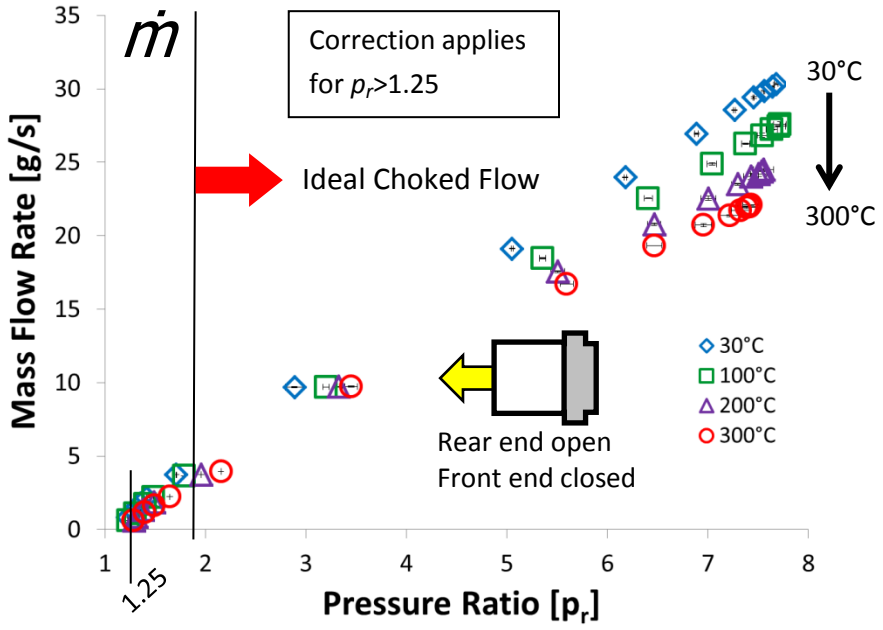

Figure 23. Measured leakage $\dot{m}$ exiting the rear of the test rig vs. pressure ratio, $p_r=P_s/P_a$. Non-rotating disk and air at four temperatures (30°C, 100°C, 200°C, and 300°C). Front end of test rig is sealed with a cap.

Appendix B lists the 4th order polynomials that fit the (rear end) parasitic leakage vs. p_r data for each temperature condition. There is no correction for measurements with pressure ratios lower than ~1.25 due to the flow meter inability to detect the small amount of leakage exiting the rear end at extremely low pressure ratios. The lowest mass flow rate recorded is ~0.6 (g/s) at p_r ~1.28. All leakage tests conducted with the test rig front end open show higher mass flow rates at p_r < 1.25; and the flow meter can detect the larger flow in the noted configuration.

Table 11 shows the inlet and exhaust conditions for the labyrinth and all-metal seal for the experiments with rotor speed.

Table 11. Air inlet and exhaust conditions for labyrinth and all-metal seal leakage measurements with rotor speed.

Specific Gas Constant	287 J/kg-K
Supply Pressure, P_s	101 kPa - 404 kPa
Inlet Temperature, T_s	303°K - 573°K
Exhaust Pressure, P_a	101 kPa
Ambient Temperature, T_a	303°K

Leakage Measurements with Labyrinth Seal

Presently, comparisons of flow rate through the labyrinth seal are shown for two conditions: one with the test rig rear end closed (same as in prior section) and the other one with the rear end open for the motor to drive the rotor shaft. In the later case, the leakage reported subtracts from the measurement the estimation of parasitic leakage (through the rear) at the same operating condition. This seal leakage is hereby reported as a *corrected* one.

Figure 24 depicts both seal leakages vs. pressure ratio and without shaft rotation. Both measurements are in good agreement when the gas temperature is ambient and at 100°C. For operation with air at 200°C and 300°C, the *corrected* seal leakage is higher than the one obtained earlier (rear end closed) by 7% and 9%, respectively.

This variance at high temperatures is attributed to the difference in air temperatures for leakage measurements with the test rig rear end closed or open and also with the seal in place. Leakage measurements performed with the test rig front end closed, as shown in Figure 23, produce the smallest flow and have the most uniform temperature as the supply pressure increases.

On the other hand, with the test rig front end open and rear end open, the supplied flow rate is much higher, the gas flows faster through the rig and prevents a steady temperature as the supply pressure increases. At temperatures well above ambient and with a large supply pressure, there is plenty of air flow that cannot be heated to the desired (set) temperature. The effect is considerable at temperatures above 200°C. Table 12 lists the uncertainties in seal leakage and pressure ratio once the *rear end* leakage is subtracted from the recorded inlet leakage.

Table 12. Uncertainties for mass flow rate and pressure ratio for measurements with a labyrinth seal after correction with rear end leakage.

	Average %	Maximum %
Mass Flow Rate	0.9	4.7
Pressure Ratio	1.2	4.6

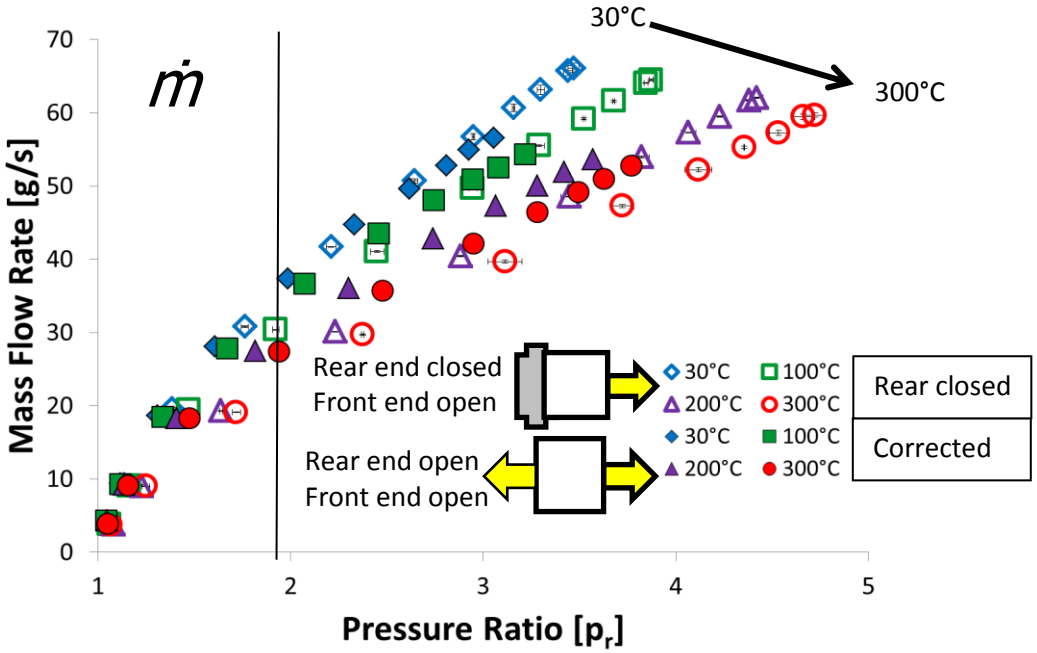

Figure 24. Labyrinth seal: mass flow rate $\dot{m}$ recorded with and without rear end of test rig closed vs. pressure ratio, $p_r=P_s/P_a$. Non-rotating disk and air at four temperatures (30°C, 100°C, 200°C, and 300°C). Discharge at ambient pressure (P_a).

Figure 25 shows the flow factor (Φ) for the labyrinth seal from measurements at 100°C and 300°C with the rotor spinning up to 2700 rpm (23.6 m/s surface speed). For immediate comparison, Figure 25 also includes the flow factor measured with the test rig rear end closed. The *corrected* flow factors at 100°C do not show a significant decrease with increasing rotor speed while the corrected flow factors at 300°C show a slight decrease with increasing rotor speed[5].

[5] The maximum rotor speed at 300°C is 2000 rpm since the motor is unable to overcome the large amount of drag on the bearings at the high temperature.

The decrease in flow factor (Φ) at 300°C is attributable to shaft speed and not to the supply temperature. The flow factor at a speed of 2000 rpm is ~2% lower than Φ at a speed of 1000 rpm, and ~4% lower than Φ taken without shaft rotation. The high temperature (300°C) makes the disk expand with rotor speed, while the results at a low temperature (100°C) do not show a decrease in Φ with increasing speed. The corrected labyrinth seal flow factors measured at 30°C and 200°C (not shown) show a similar trend to the results at 100°C. Note that Φ for the measurements conducted with the rear end of the test rig closed approach each other as the pressure ratio increases.

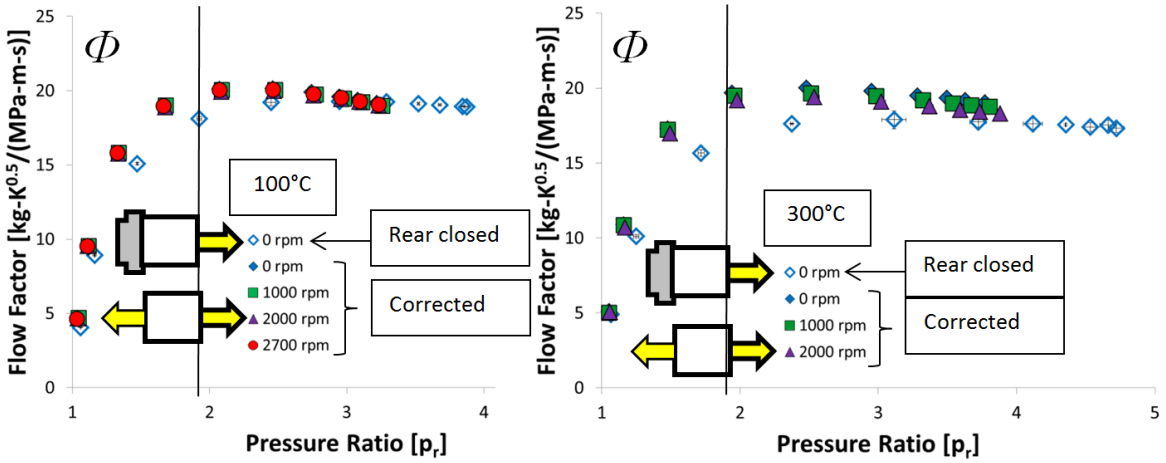

Figure 25. Labyrinth seal: flow factor Φ recorded vs. pressure ratio, $p_r=P_s/P_a$. Rotor speeds of 1 krpm, 2 krpm and 2.7 krpm and air at two temperatures (100°C and 300°C). Discharge at ambient pressure (P_a). For comparison: leakage measurement with rear end of test rig closed shown (0 rpm).

Leakage Measurements with All-metal Seal

Figure 26 shows the *corrected* leakage compared to the measured leakage with the rear end of the test rig closed. The measurements are taken without shaft rotation. The leakage begins to level off for $p_r > 3$, the limit for the radial travel of the pads being drawn to the disk as the supply pressure increases.

The leakage recorded for inlet gas temperatures at 200°C and 300°C are similar. This effect is caused by the pads reaching the closest distance to the disk as a result of both

thermal expansion and supply pressure. Thus, the leakage cannot be reduced much further with the novel seal after reaching 200°C.

The *corrected* seal leakage data at 100°C, 200°C, and 300°C are in good agreement with the measured leakage with the test rig rear end closed. On the other hand, the *corrected* leakage at 30°C is ~70% (6 g/s) higher from p_r=2 to 3 and ~40% (3.5 g/s) higher at p_r=3.75 than the measured leakage with the rig rear end closed. The *corrected* leakage at 30°C begins to converge towards the measured leakage with the rig rear end closed for $p_r > 3$.

The flexible pads may be the cause of this behavior at low temperatures when the all-metal seal is tested. At high temperature, the allowable radial movement of the flexibly mounted pads decreases since the pads and disk undergo thermal expansion. This limiting effect is evident in the leakage measurements taken at 200°C and 300°C where the leakage barely decreases. The pads can deflect a greater distance at a low temperature of 30°C since the thermal expansion of the components is minimal. Table 13 lists the uncertainties in seal leakage and pressure ratio once the *rear end* leakage is subtracted from the recorded inlet leakage.

Table 13. Uncertainties for mass flow rate and pressure ratio for measurements with all-metal seal after correction with rear end leakage.

	Average %	Maximum %
Mass Flow Rate	0.6	8.4
Pressure Ratio	0.8	3.9

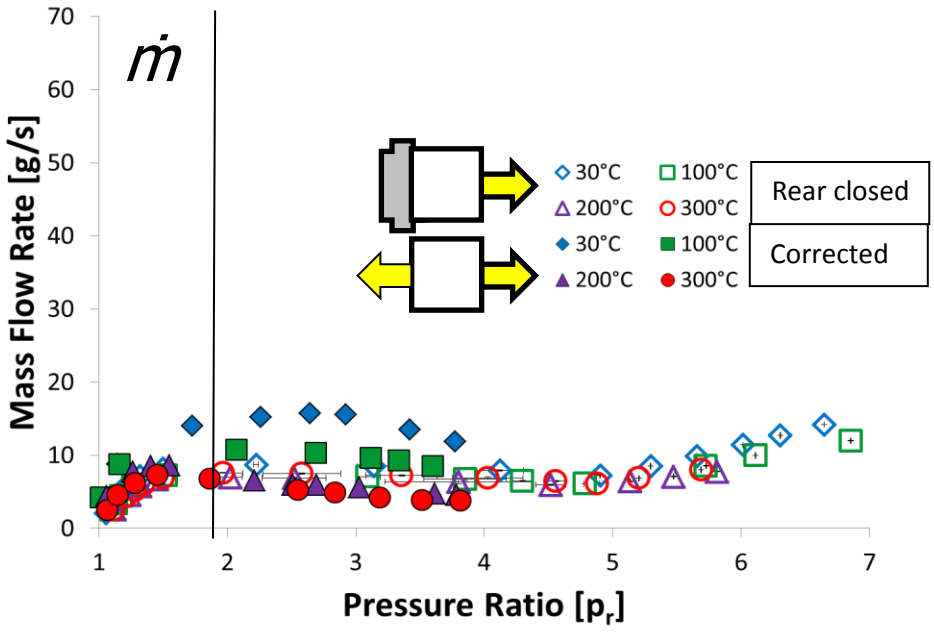

Figure 26. All-metal seal: mass flow rate $\dot{m}$ recorded vs. pressure ratio, $p_r=P_s/P_a$. Non-rotating disk and air at four temperatures (30°C, 100°C, 200°C, and 300°C). Discharge at ambient pressure (P_a). For comparison: leakage measurement with rear end of test rig closed shown (0 rpm).

Figure 27 shows the flow factor (Φ) for the all-metal seal from measurements with air inlet temperature at 30°C and 100°C and with the rotor spinning with speeds up to 2700 rpm. Figure 27 also includes the flow factor measured with the rear end closed for comparison. In general, near the pressure ratio for choking, Φ at 30°C for the lowest shaft speeds (0 and 1000 rpm) is up to ~10% higher than that for the higher rotor speeds (2000 and 2700 rpm) . Φ measured at 100°C and 0 rpm is slightly larger than those at higher shaft speeds. The flow factor for the measurements conducted with the rear end of the test rig closed is lower than the corrected flow factor for both temperature conditions.

The flow factor for the measurements conducted with the rear end closed approaches the *corrected* flow factor as the pressure ratio increases. The flow factor for the labyrinth seal also shows this behavior.

There is a large difference in leakage at low pressure ratios, p_r<1.25, due to the limitation in the flow meter.

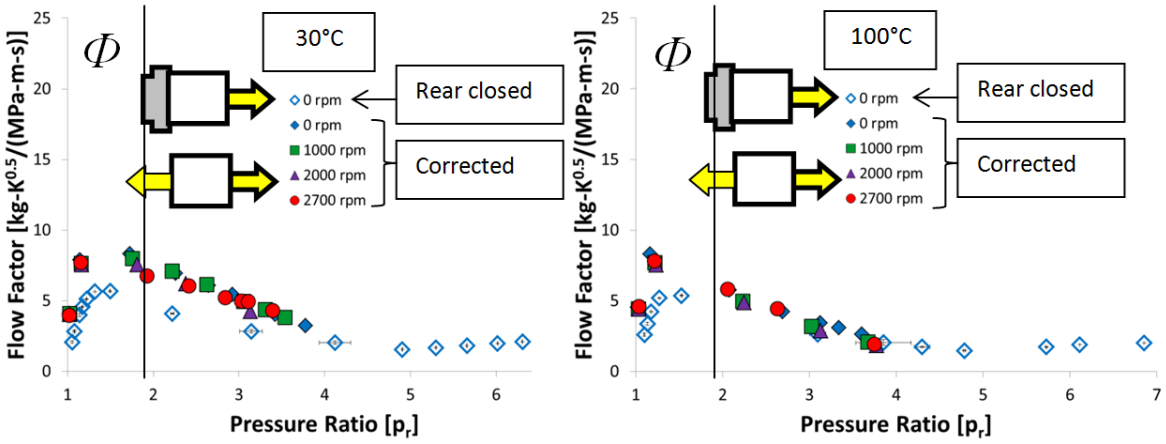

Figure 27. All-metal seal: flow factor Φ recorded vs. pressure ratio, $p_r=P_s/P_a$. Rotor speeds of 1 krpm, 2 krpm and 2.7 krpm and two temperatures (30°C and 100°C). Discharge at ambient pressure (P_a). For comparison: leakage measurement with rear end of test rig closed shown (0 rpm).

Figure 28 shows the comparison between flow factors Φ with air at 200°C for a stationary shaft and also spinning at 1,000 rpm[6]. The limited range of pressure ratios show a decrease in flow factor with an increase in rotor speed. For example, at 0 rpm Φ is ~20% higher than the flow factor at 1000 rpm at a pressure ratio of 3.2.

[6] The maximum rotor speed at 200°C is 1000 rpm since the motor is unable to overcome the large amount of drag on the bearings at the high temperature. Measurements at 300°C could not be conducted with rotor speed for the all-metal seal.

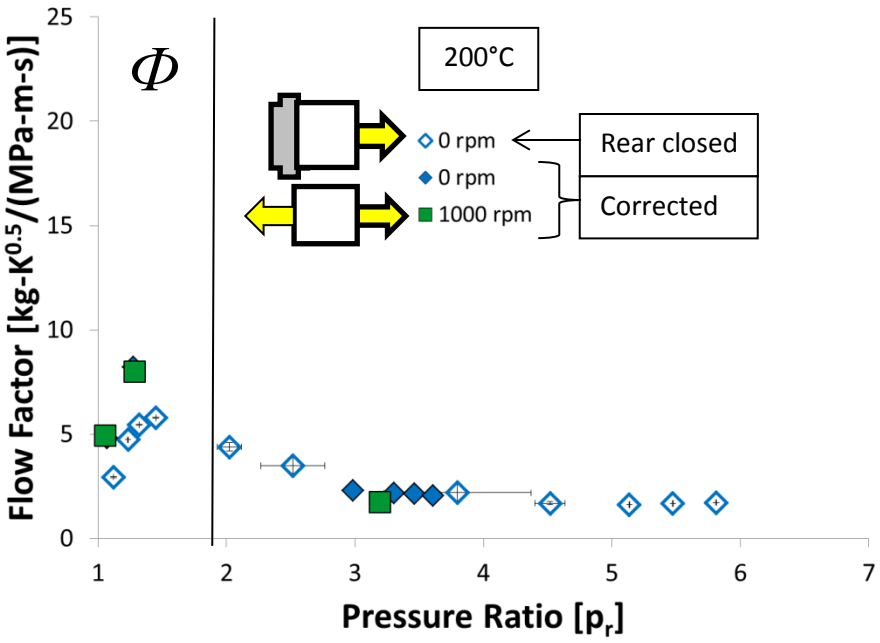

Figure 28. All-metal seal: flow factor *Φ* recorded vs. pressure ratio, $p_r=P_s/P_a$, with air inlet at 200°C. Stationary disk and spinning at 1 krpm. Discharge at ambient pressure (P_a). For comparison: leakage measurement with rear end of test rig closed shown (0 rpm).

CHAPTER IX

SEAL DRAG TORQUE MEASUREMENTS

In addition to minimizing leakage, seals with a low power loss due to reduced drag conserve energy and extend the life of components. A low amount of heat generation is a direct cause of minimal drag. In general, the power loss in a non-contacting seal increases with increasing surface speed and area exposed.

A mechanical power loss equals the drag torque (T_o) times rotational speed (ω). In the current test system, rolling friction in the rolling element bearings, drag friction in the metal mesh foil bearing, and windage on the disk increase the torque the motor needs to deliver to produce rotation. Air windage induced power loss increases dramatically with surface speed, air density (and pressure) [21], and is proportional to the *wetted* area from the disk surface (~200 cm^2). In addition, a large supply pressure into the test rig chamber produces a high axial force, F, which pulls on the shaft and loads the bearings excessively. The latter effect shows dramatically with a large increase in torque just to initiate the rotation of the disk, i.e., it is most vivid at a low speed condition.

A direct current (DC) power supply (48 V, 2 A max.) powers the motor that spins the shaft-disk system up to 1.8 krpm. Furthermore, three automotive DC batteries connected in series provide an additional 36 V to ramp up the rotor speed to 2.7 krpm. At this speed, the disk surface speed is 23.6 m/s. The batteries are fully charged prior to each test and the necessary voltage is maintained by adjusting the output voltage of the power supply. Electrical power ($\wp$) equals voltage (V) times current (i). The mechanical power equals the electrical power under the assumption that all of the electrical energy is converted into mechanical energy (no electro mechanical losses). Although there are losses during the test rig operation, this assumption provides a simple methodology to gather, calculate, and compare various power and torque behavior for both seals.

Without a seal in place, the baseline drag torque (T_o) is a result of disk windage as well as drag torque produced by the support tapered roller bearings and the metal mesh foil bearing. The baseline torque is derived from measurements of voltage (V) and current (i) with the test rig operating at ambient temperature and without external pressurization. Measurements are taken from 200 rpm to 2000 rpm at 200 rpm increments. Three separate measurements are

obtained at each condition to ensure repeatability. Equating the mechanical power ($\wp$) to the electrical power, $T_o\ \omega = V\ i$; then $T_o = k_{V\omega}\ i$, with $k_{V\omega} = V/\omega$ as the motor constant = 0.2394 V/(rad/s), as shown in Figure 29.

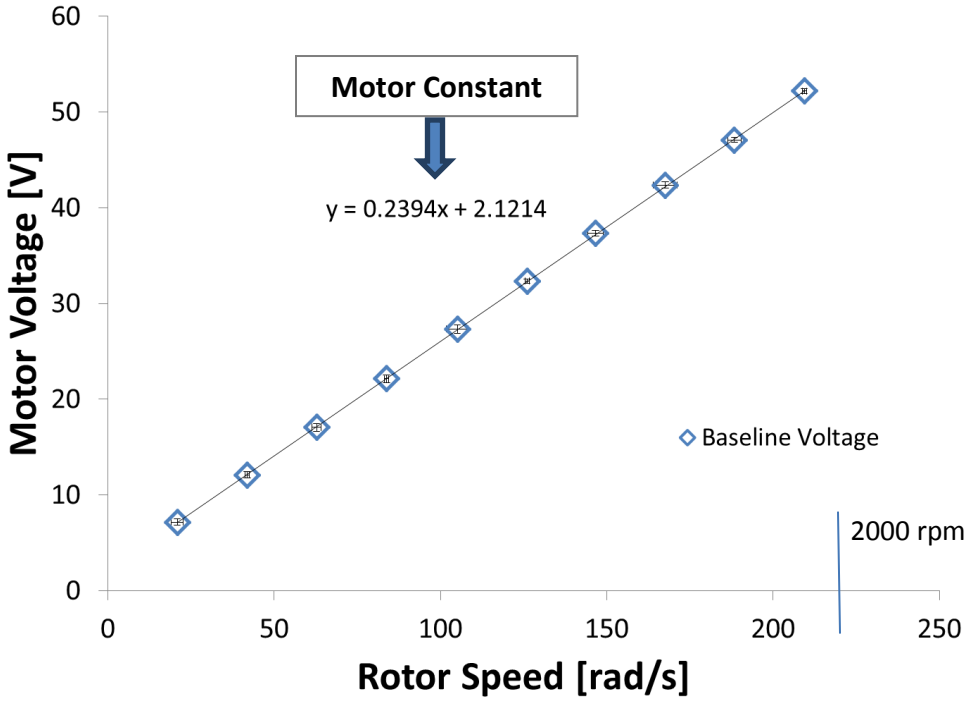

Figure 29. Electrical motor voltage vs. rotor speed. No seals installed. No external pressurization, air at ambient temperature.

Figure 30 shows the derived baseline electrical motor power and torque versus rotor speed. No seal is installed in the test rig and no external pressure is fed into the rig chamber. The baseline motor torque is ~0.45 N-m at a low speed, ~0 rpm, decreases slightly to ~0.4 N-m at a speed of 500 rpm, and then gradually increases with rotor speed until reaching a constant 0.5 N-m at 2000 rpm. The baseline motor power increases with rotor speed, and is only ~100 W at the highest speed (2 krpm).

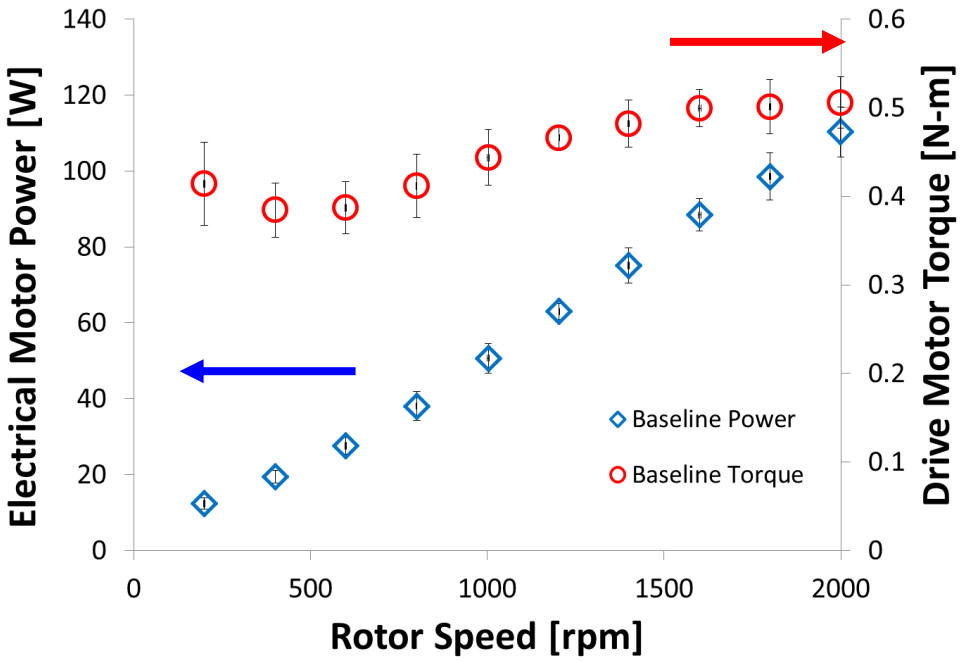

Figure 30. Baseline electrical motor power and drive motor torque vs. rotor speed. No seals installed. No external pressurization, air at ambient temperature.

With the test seals in place, Figures 31 and 32 depict the electrical power $\left(\wp = iV\right)$ and the *estimated* torque, $T_o = \wp/\omega$, to drive the test rig for increasing rotor speeds and three supply pressures, p_r = 1, 2, and 3. The measurements show independent tests with the labyrinth seal first, and then with the all-metal seal installed. The reported torque includes the dry-friction torque from the roller bearings supports, the metal mesh foil bearing, disk windage, and to a minor extent, the drag torque from the seal. The disk windage and drag on the tapered roller bearings increase the torque significantly when there is external pressurization.

The electrical power appears to increase linearly with rotor speed, $\wp \sim \omega$, which signifies the importance of a nearly constant torque for all speeds, low and high. At the lowest rotational speed, the system torque increases dramatically with the supply pressure. This torque is denoted as a "breakaway" torque that represents the static torque the motor needs to overcome so that disk rotation ensues. The torque at 200 rpm is ~0.4 N-m at p_r=1, ~0.8 N-m

at p_r=2, and ~1.5 N-m at p_r =3. Since the rotational speed is so slow, this breakaway torque must come only from hard contact at the bearing supports.

The tests evidence the same torque, irrespective of the seal installed, as the uncertainty bars show. For tests with p_r=1, i.e., without supply pressure, the drag torque increases with rotor speed to reach ~0.5 N-m at 2 krpm. In contrast, for tests with external pressurization, the mechanical torque drops with rotor speed. The evidence is more dramatic for the condition with p_r=3 that shows the torque decreases at a faster rate than for tests at p_r=2. The rationale for the drop is elusive. It is plausible that as the shaft speed increases, the leakage thru the rear end of the test rig produces a lubrication effect that reduces the drag. At high speeds, the power deviates from being proportional to shaft speed which denotes a drop in drive torque, as shown in Figure 32. For both seals, Table 14 lists the average and maximum uncertainty in electrical power, drive torque and rotor speed measurements.

Table 14. Uncertainties for measured electrical power, torque and rotor speed for tests with a labyrinth seal and an all-metal seal.

	Labyrinth Seal		All-Metal Seal	
	Average %	Maximum %	Average %	Maximum %
Power	8.4	19.2	6.9	22.1
Torque	7.1	14.8	5.7	19.8
Speed	0.4	1.5	0.5	2.3

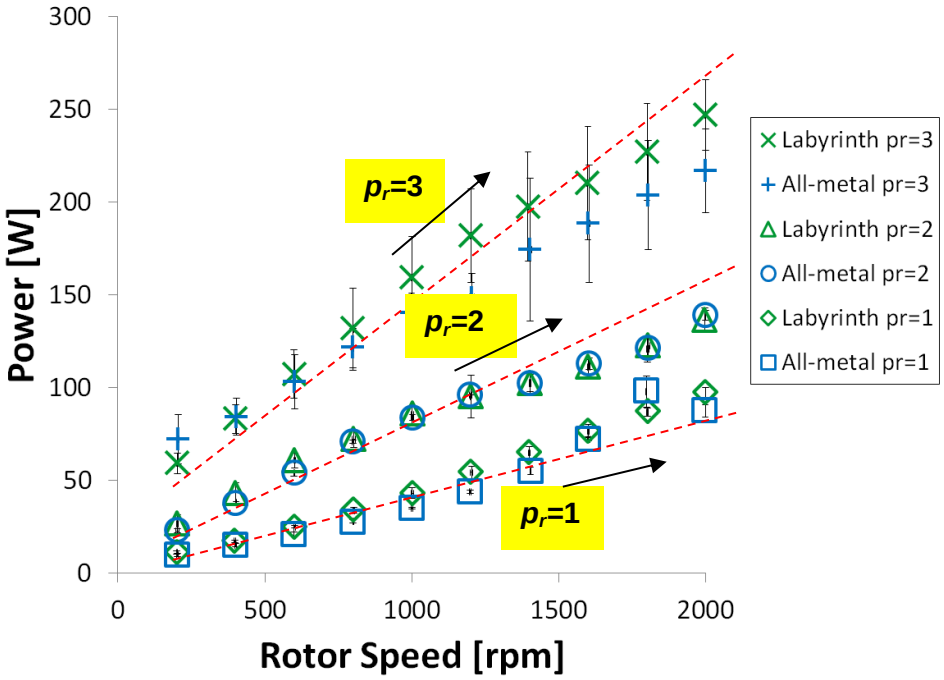

Figure 31. Electrical power for the test rig with seals installed (a labyrinth seal and an all-metal seal) vs. rotor speed. Air at ambient temperature and three inlet pressures, p_r=1, 2, 3.

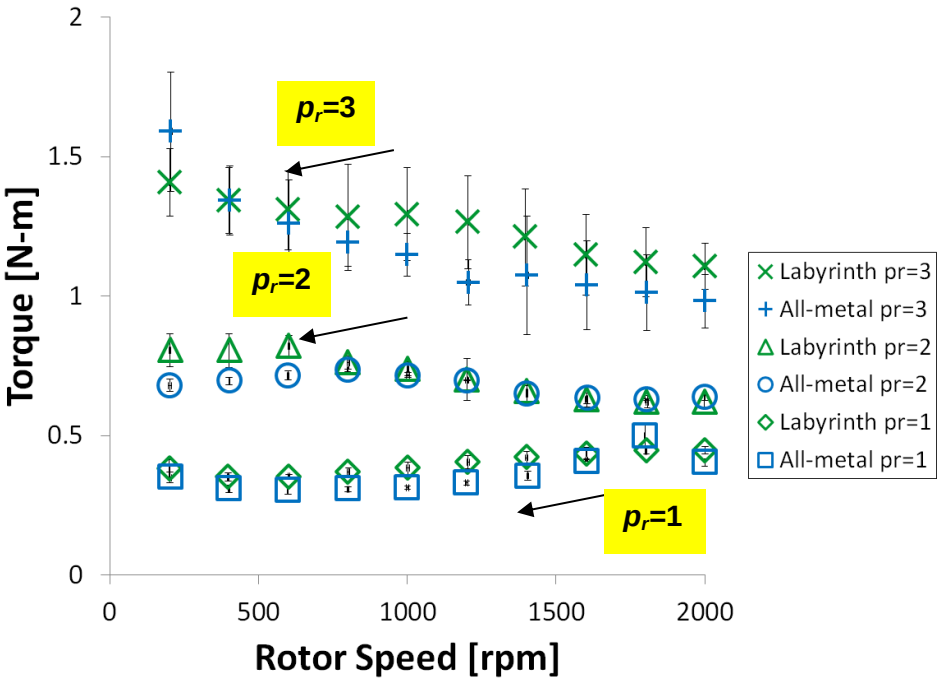

Figure 32. Derived torques for test rig with seals installed (a labyrinth seal and an all-metal seal) vs. rotor speed. Air at ambient temperature and three inlet pressures, p_r=1, 2, 3.

Figure 33 shows the differences in torque, i.e., system torque with a labyrinth seal in place minus the torque with an all-metal seal in place versus speed and three pressure supply conditions, p_r = 1, 2, and 3. Positive data points correspond to higher estimated torque with a labyrinth seal in place. There is no consistent trend since all torque differences are less than the uncertainty band so the torque caused by a seal cannot be determined with any accuracy.

Theoretically, the labyrinth seal should have the lowest torque since it has the largest clearance and, thus, will offer the lowest resistance to shear drag. The measurements, however, show both seals produce the same drag torque (within the uncertainty bounds). This drag torque is a small fraction of the overall motor torque driving the test rotor. The largest torque arises from friction in the support ball bearings.

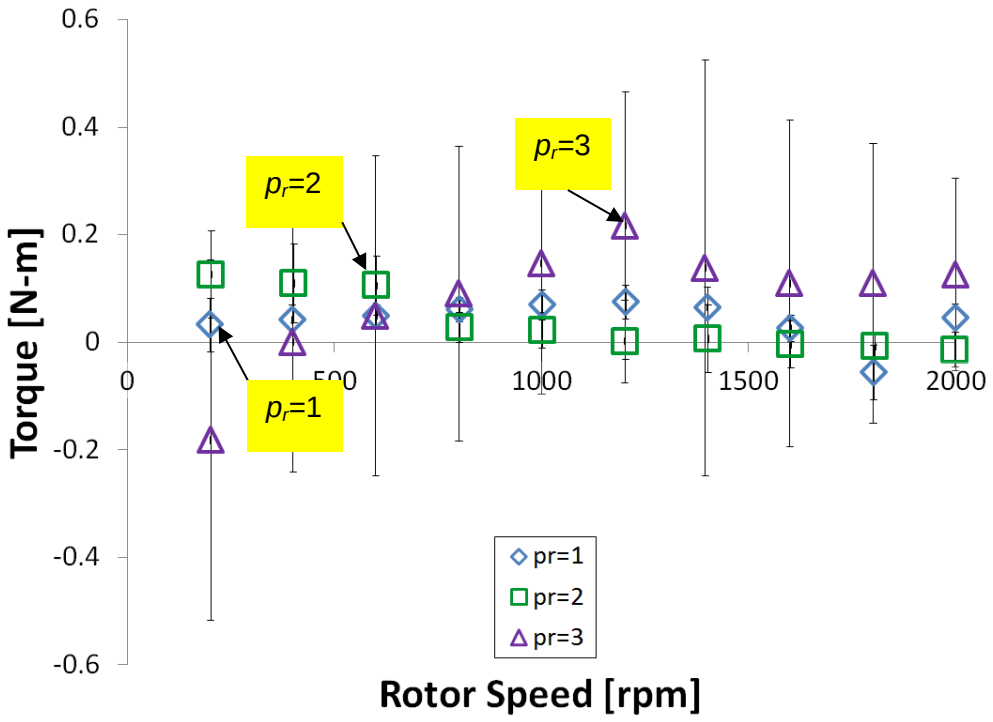

Figure 33. Estimated torque difference for tests in rig with seals installed (a labyrinth seal and an all-metal seal) vs. rotor speed. Air at ambient temperature and three inlet pressures, p_r=1, 2, 3.

CHAPTER X

CONCLUSIONS AND RECOMMENDATIONS

Labyrinth seals are the most common and inexpensive seal type, albeit wearing out with operation thus penalizing performance and even affecting rotordynamic stability. Novel sealing technology outperforms labyrinth seals in terms of leakage. At present, there are other seal types that have low drag power losses and are more effective at reducing leakage. Industries seeking to increase efficiency by reducing (parasitic) secondary leakage losses can benefit greatly by a change in seal technology [2].

Parasitic secondary flow losses (seal leakage) reduce efficiency and power delivery in turbomachinery. The all-metal seal is a novel seal type, originating from the HBS, as a softly supported, multiple-pad seal with both hydrostatic and hydrodynamic lift characteristics to generate a self-controlling clearance seal.

Static leakage tests with both a labyrinth seal and a novel all-metal seal at high temperature (max. 300°C) show the novel seal provides at least a 70% decrease in leakage above a pressure ratio (P_s/P_a) of 2. These seals are more effective at withstanding higher pressure differentials than labyrinth seals do. The novel seal leaks ~1/5 the flow in a labyrinth seal for pressure ratios (P_s/P_a) > 3.5, thus demonstrating its excellent sealing characteristics.

The flow factor (Φ) for the all-metal seal reaches ~2 kg-$K^{0.5}$/(MPa-m-s) at a high temperature (max. 300°C) and pressure ratios (P_s/P_a) > 3.5, while the labyrinth seal reaches a flow factor (Φ) ~17.5 kg-$K^{0.5}$/(MPa-m-s) under the same test conditions. Hence, the all-metal seal has 11% of the flow factor of a similarly sized labyrinth seal for operation at pressure ratios (P_s/P_a) > 3.5. The dramatic reduction in leakage is greatest for operation with large pressure differentials.

Clearance measurements for the labyrinth seal show a slight decrease (~15%) in clearance with increasing temperature (up to 300°C). A simple model developed to account for thermal expansion of the multiple components and the small gap between the seal outer diameter and housing groove concurs with the experimental clearance measurements. The decrease in clearance is a leading factor of the decrease in leakage as the temperature increases.

The measured clearances are used to predict the leakage at various temperatures and pressures using XLLaby1CV®, a predictive code for gas labyrinth seals developed by Thorat [20]. The predictions also agree closely with the static experimental leakage measurements of the labyrinth seal.

Leakage measurements with a rotor spinning to a maximum speed of 2700 rpm (surface speed = 23.6 m/s) show a decrease in leakage with increasing rotor speed. Rotor speed has a minor effect on the flow factor for the labyrinth seal, at both low and high temperatures. For example, at 300°C, the labyrinth seal flow factor for tests at 2 krpm is ~4% lower than the flow factor for tests without shaft rotation.

The novel seal experiences a much larger percentage decrease in flow factor with increasing speed for all recorded temperatures (30°C, 100°C, and 200°C). In general, the seal flow factor at a pressure ratio of ~1.89 (ideal choke condition) and at 30°C for the lowest speeds (0 and 1000 rpm) is up to 10% greater than at the highest rotor speeds (2000 and 2700 rpm). The flow factor at 0 rpm is ~20% higher than the flow factor at 1000 rpm at a pressure ratio of 3.2 and at a temperature of 200°C.

Measurements of the electrical power in the motor driving the test rig to a maximum speed of 2000 rpm (surface speed = 17.5 m/s) show that the test system has a large static *breakaway* torque that increases with the magnitude of air pressurization in the vessel upstream of the test seal. Hence, the motor drive torque derived from the electrical power includes the effect of not only the seal installed, but also windage (air drag) from the large surface rotating disk, drag in the metal mesh foil bearing, and an overwhelming (friction) torque from an increasing axial preload in the support rolling element bearings as the supply pressure rises. Efforts to isolate the drag torque due to a test seal alone were futile because of the large uncertainty and lack of repeatability of the measurements.

The all-metal seal acts with hydrostatic and hydrodynamic effects that draw the pads close to the rotor to restrict gas leakage. The all-metal seal produces a fraction of the leakage that a conventional labyrinth seal will have, in particular at high pressure differentials. Tests with increasing rotor speed show a minor reduction in leakage for both the all-metal seal and the labyrinth seal. The all-metal seal is recommended over conventional straight through labyrinth seals in high pressure environments or where extreme leakage reduction is a primary objective, as in gas and steam turbines, for example.

Further improvements on the current test rig include installing a more powerful motor which can deliver a large torque, installing angular contact ball bearings to support the shaft, and also selecting a more sensitive flow meter. The current tapered roller bearings must be tightly installed to prevent large shaft axial displacements. A more sensitive flow meter will record small flow rates typical for the all-metal seal and for the parasitic leakage exiting through the rear of the test rig. A torque meter can be connected to the transmission shaft to directly measure torque in contrast to measuring the drive motor current and voltage. The drag torque from a seal can be determined from measurements with and without a seal in place and as shaft speed changes. The method applies only when there is no air pressurization.

REFERENCES

[1] Chupp, R. E., Hendricks, R. C., Lattime, S. B., and Steinetz, B. M., 2006, "Sealing in Turbomachinery," AIAA J. Propul. Power, **22**(2), pp. 313-349.

[2] Chupp, R. E., Johnson, R. P., and Loewenthal, R. G., 1995, "Brush Seal Development for Large Industrial Gas Turbines," AIAA Paper No. 1995-3146.

[3] Justak, J., and Doux, C., 2009, "Self-Acting Clearance Control for Turbine Blade Outer Air Seals," ASME Paper No. GT2009-59683.

[4] San Andrés, L., and Ashton, Z., 2010, "Comparison of Leakage Performance in Three Types of Gas Annular Seals Operating at a High Temperature (300°C)," Tribol. Trans., **53**(3), pp. 463-471.

[5] San Andrés, L., and Anderson, A., 2011, "Comparison of Leakage Between a Labyrinth Seal and an All-Metal Compliant Gas Seal at High Temperature," Report to TRC-S-02-2011, Turbomachinery Research Consortium, Texas A&M University, May.

[6] Delgado, I. R., and Proctor, M. P., 2006, "Continued Investigation of Leakage and Power Loss Test Results for Competing Turbine Engine Seals," AIAA Paper No. 2006-4754.

[7] Eser, D., and Kazakia, J. Y., 1995, "Air Flow in Cavities of Labyrinth Seals," Int. J. Eng. Sci., **33**(15), pp. 2309-2326.

[8] Floyd, C. G., 1986, "Gas Seals for Rotating Shafts," Tribol. Int., **19**(4), pp. 204-211.

[9] Childs, D. W., 1993, *Turbomachinery Rotordynamics: Phenomena, Modeling and Analysis*, John Wiley & Sons, New York, NY, Chap 5.

[10] Justak, J. F., and Crudgington, P. F., 2006, "Evaluation of a Film Riding Hybrid Seal," AIAA Paper No. 2006-4932.

[11] El-Gamal, H. A., Awad, T. H., and Saber, E., 1996, "Leakage from Labyrinth Seals Under Stationary and Rotating Conditions," Tribol. Int., **29**(4), pp. 291-297.

[12] Ferguson, J. G., 1988, "Brushes as High Performance Gas Turbine Seals," ASME Paper No. 88-GT-182.

[13] Hendricks, R. C., Carlile, J. A., Liang, A. D., 1993, "Brush Seal Low Surface Speed Hard-Rub Characteristics," AIAA Paper No. 1993-2534.

[14] Delgado, A., San Andrés, L., Justak, J. F., 2005, "Measurements of Leakage, Structural Stiffness and Energy Dissipation Parameters in a Shoed Brush Seal," SealingTechnol., **2005**(12), pp. 7-10.

[15] San Andrés, L., Baker, J., and Delgado, A., 2009, "Measurements of Leakage and Power Loss in a Hybrid Brush Seal," ASME J. Eng. Gas Turbines Power, **131**(1), p. 012505.

[16] San Andrés, L., and Ashton, Z., 2009, "Monthly Report No. 16: May," Proprietary Technical Report to Siemens Power Gen., TEES Project 32525/34650/ME, Turbomachinery Laboratory, Texas A&M University.

[17] Ashton, Z., 2009, "High Temperature Leakage Performance of a Hybrid Brush Seal Compared to a Standard Brush Seal and a Labyrinth Seal," M.S. thesis, Texas A&M University, College Station, TX.

[18] San Andrés, L., Chirathadam, T. A., Kim, T., 2010, "Measurement of Structural Stiffness and Damping Coefficients in a Metal Mesh Foil Bearing," ASME J. Eng. Gas Turbines Power, **132**(3), p. 032503.

[19] San Andrés, L., Chirathadam, T. A., Ryu, K., and Kim, T.H., 2010, "Measurements of Drag Torque, Lift-Off Journal Speed and Temperature in a Metal Mesh Foil Bearing," ASME J. Eng. Gas Turbines Power, **132**(11), p. 112503 (1-7).

[20] Thorat, M. R., 2010, "Impact of Rotor Surface Velocity, Leakage Models and Real Gas Properties on Rotordynamic Force Predictions of Gas Labyrinth Seals," M.S. thesis, Texas A&M University, College Station, TX.

[21] Bruckner, R. J., 2009, "Windage Power Loss in Gas Foil Bearings and the Rotor-Stator Clearance of High Speed Generators Operating in High Pressure Environments," NASA/TM-2009-215826.

[22] John, J. E., and Keith, T. G., 2006, *Gas Dynamics: Third Edition*, Pearson Prentice Hall, Upper Saddle River, NJ, Chap 3.

APPENDIX A

CALIBRATION OF DISPLACEMENT SENSORS

Two displacement sensors measure the horizontal and vertical distance of the disk. The calibration setup for the sensors is shown in Figure A.1. A lathe is used to secure the disk in place while the sensor is mounted perpendicular to the disk with a magnetic stand. The sensor is placed very close to the disk and the position is set at a zeroed position. The sensors are then moved away from the disk at 0.1 mm increments to obtain the sensitivity.

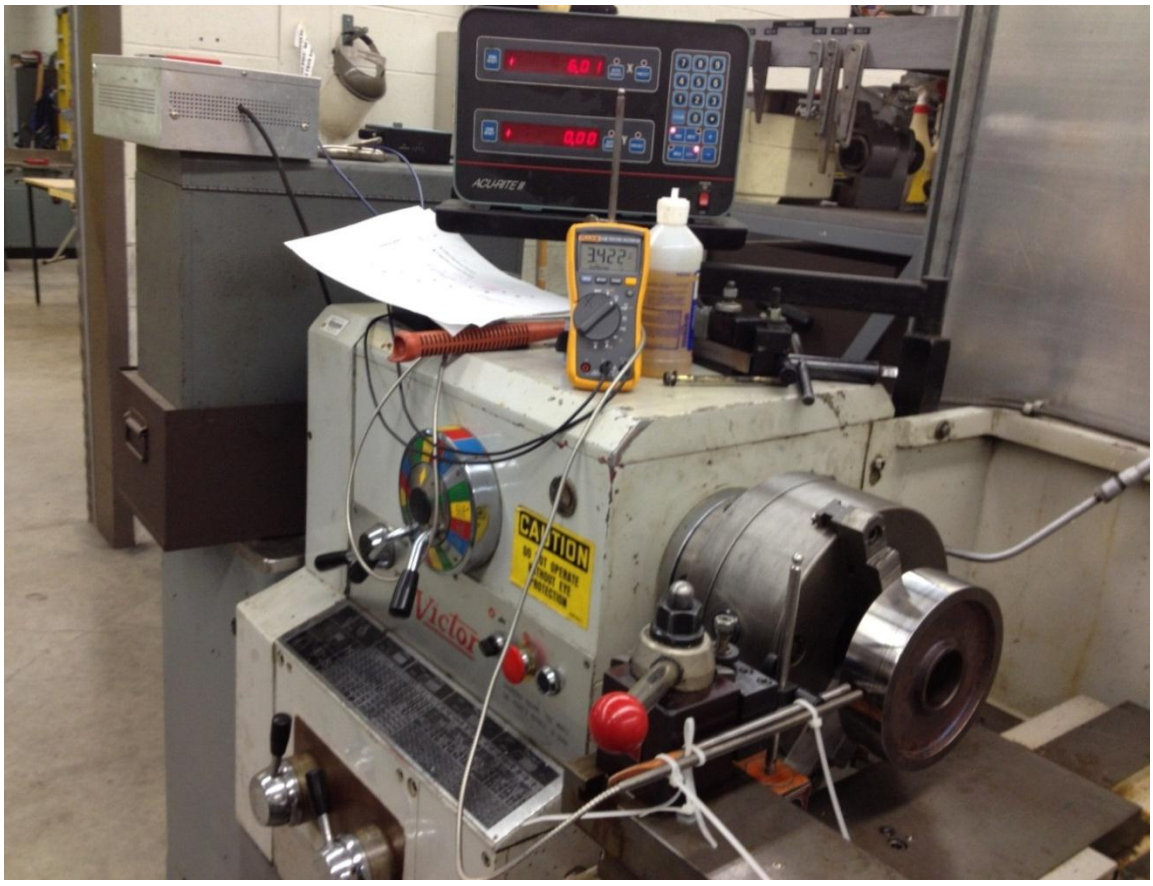

Figure A.1. The sensor and disk are positioned on a lathe during the calibration procedure.

The sensors output a voltage proportional to the distance from the disk. Data is taken until the sensor is out of range. The data is then processed to display the linear portion of the measurements only. It is important for the sensors to be operating within the range of voltage

of the linear data. Figure A.2 shows the displacement versus voltage for both sensors. The horizontal sensor is slightly bent and has a substantially larger sensitivity than the vertical sensor. The labyrinth seal and all-metal seal have small diametrical clearances (0.51 mm and 0.43 mm) with the disk which are within the linear range of the sensitivities of both sensors. The manufacturer lists the typical sensitivity as 0.45 mm/V (+/- 15%) and will vary with the surface finish and reflectivity of the target.

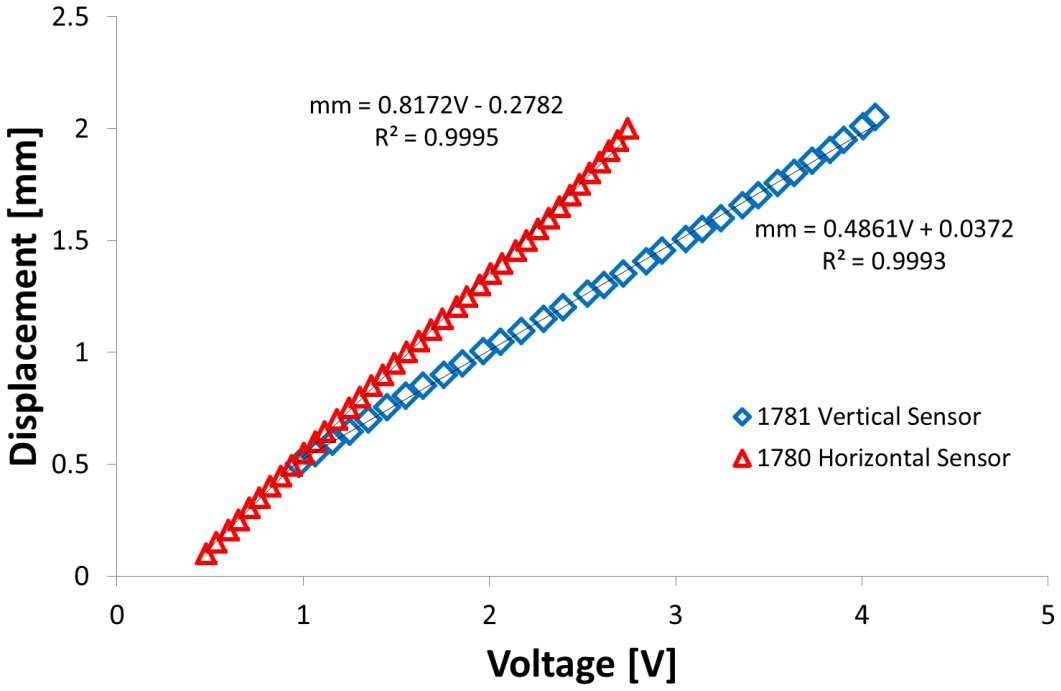

Figure A.2. Experimentally determined vertical and horizontal sensor sensitivities.

APPENDIX B

POLYNOMIAL EQUATIONS DERIVED FROM LEAKAGE MEASUREMENTS TAKEN WHEN THE FRONT OF THE TEST RIG IS SEALED WITH A CAP

There is a small gap around the shaft which allows the shaft to rotate when connected to the drive motor. Quantifying the leakage though the rear end of the test rig is necessary to determine the leakage exiting through the seal installed during tests with a spinning rotor.

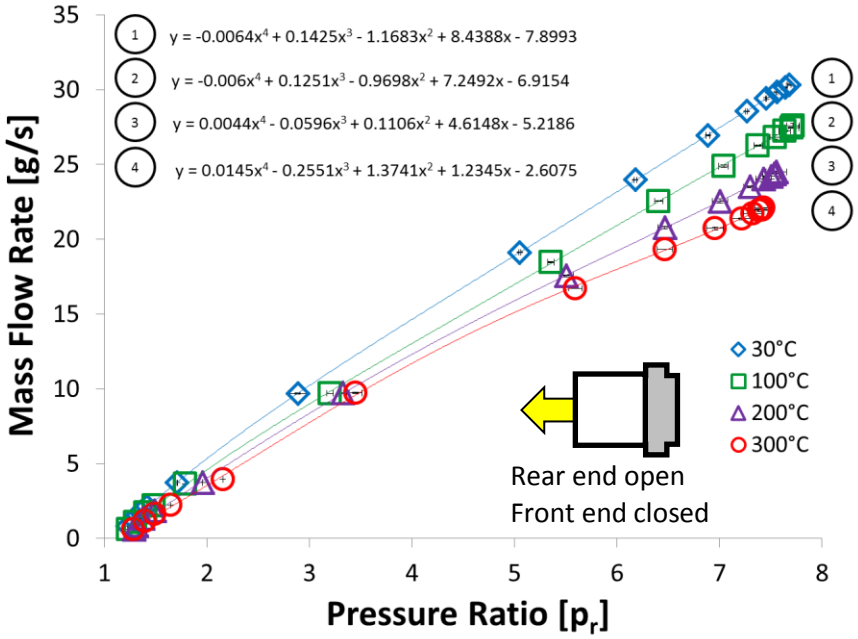

Figure B.1. Polynomial equations depicting the measured leakage $\dot{m}$ exiting the rear end of the test rig vs. pressure ratio, $p_r=P_s/P_a$. Non-rotating disk and air at four temperatures (30°C, 100°C, 200°C, and 300°C). Front end of test rig is sealed with a cap.

Figure B.1. shows the leakage exiting the rear end versus pressure ratio for tests with air at four temperatures. The test data for the parasitic leakage at a fixed temperature is curve fitted as a fourth order polynomial, i.e.

$$\dot{m}_{rear} = \sum_{x=0}^{4} a_x p_r^x \qquad \text{(B. 1)}$$

The seal leakage ($\dot{m}$) in g/s equals to the total leakage (Q) minus the leakage through the rear end,

$$\dot{m} = Q - \dot{m}_{rear} \tag{B. 2}$$

The curve fit formulas obtained for each temperature condition are:

$$\dot{m}_{30°C} = Q - (-0.0064p_r^4 + 0.1425p_r^3 - 1.1683p_r^2 + 8.4388p_r - 7.8993) \tag{B. 3}$$

$$\dot{m}_{100°C} = Q - (-0.006p_r^4 + 0.1251p_r^3 - 0.9698p_r^2 + 7.2492p_r - 6.9154) \tag{B. 4}$$

$$\dot{m}_{200°C} = Q - (0.0044p_r^4 - 0.0596p_r^3 + 0.1106p_r^2 + 4.6148p_r - 5.2186) \tag{B. 5}$$

$$\dot{m}_{300°C} = Q - (0.0145p_r^4 - 0.2551p_r^3 + 1.3741p_r^2 + 1.2345p_r - 2.6075) \tag{B. 6}$$

APPENDIX C

CALIBRATION OF PRESSURE SENSORS AND FLOW METER

Pressure Sensors

Three pressure sensors are used in the test rig to record the pressure upstream of the flow meter, the supply pressure (P_s) in the pressurized vessel and the exit pressure (P_a). A high temperature pressure sensor is located in the hot air inlet pipe leading to the pressurization chamber to gather P_s.

Figure C.1 shows the calibration data, voltage versus pressure for the high temperature pressure sensor (max. operating temperature of 300 °C). The sensor is calibrated using a dead weight tester to maximum static pressures of 100 psig. The sensor is linear (perfect line curve fit) with a sensitivity of 242.2 psig/V. The bias or linearity, uncertainty is +/- 0.25% full-scale output (FSO) and the precision or repeatability uncertainty is +/- 0.1% FSO.

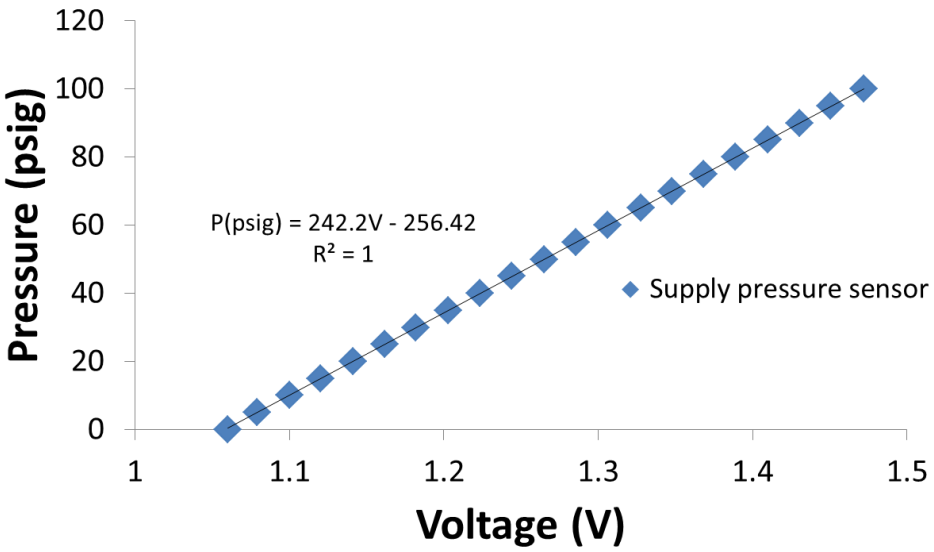

Figure C.1. Voltage versus static pressure for pressure sensor to record supply pressure in high temperature gas seal test rig.

Two miniature (Kulite) pressure sensors collect pressures at the flow meter location and the exhaust location. Figure C.2 displays the calibration voltage versus pressure data collected for both sensors to a maximum static pressure of 125 psig using a dead weight

tester. The sensors require of a power supply at a well-known voltage. The pressure sensor at the flow meter and the pressure sensor at the exhaust side require a DC power supply of 10.77 Volts. Changes in the supplied voltage will cause the sensor gain to change. The sensors linearity is 1 (flow meter) and 0.99 (exhaust) while their sensitivity is 959 psig/V (flow meter) and 1114 psig/V (exhaust). The Kulite sensors have a combined non-linearity and hysteresis uncertainty of +/-0.1 FSO and a precision uncertainty of +/-0.5% FSO.

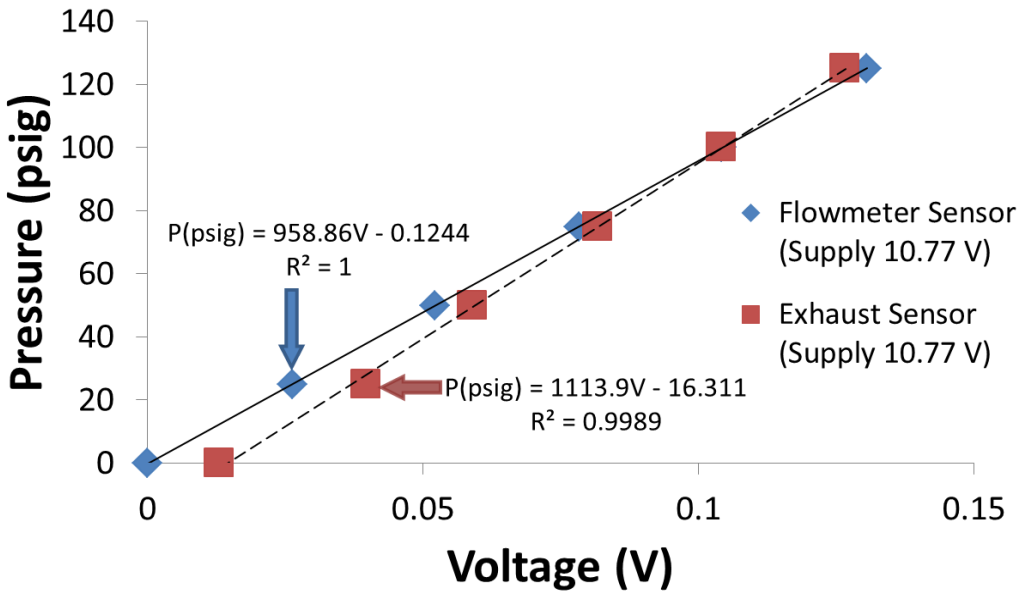

Figure C.2. Pressure vs. output voltage for miniature pressure sensors at specified output voltages. Air at ambient temperature.

Turbine Flow Meter

Figure C.3 shows the manufacturer calibration data for the turbine flow meter (Flow Technology Inc., SN 120872, and Model number FT-12NEYABGEH-5). The flow rate measurements must be conducted at ambient temperature and with at an upstream pressure of 100 psig just before the flow meter. The manufacturer given sensor uncertainty is +/-0.2 SCFM.

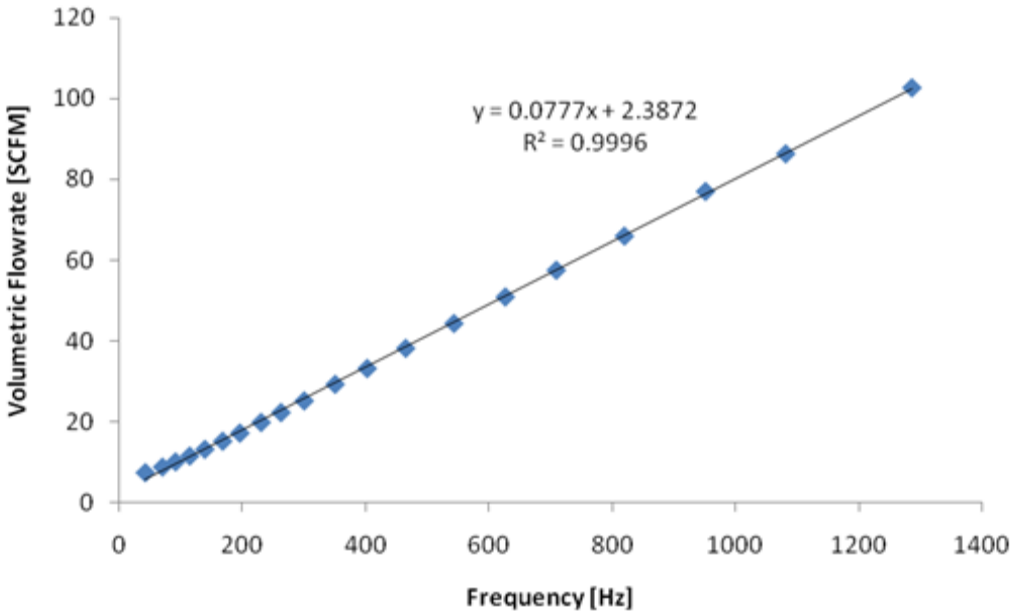

Figure C.3. Volumetric flow rate (SCFM) versus frequency (Hz) in turbine flow meter.

APPENDIX D

VOLUMETRIC FLOW RATE MEASUREMENTS WITH A LABYRINTH SEAL – NO ROTOR SPINNING

Figure D.1 shows the volumetric flow rate, $Q = \frac{\dot{m}}{\rho}$, versus pressure ratio for the labyrinth seal. The figure shows Q increases slightly with an increase in absolute temperature. Q remains constant after reaching the choke pressure ratio. The air density is determined by using the ideal gas law and varies with the supply pressure and temperature, $\rho = \frac{P_s}{RT_s}$.

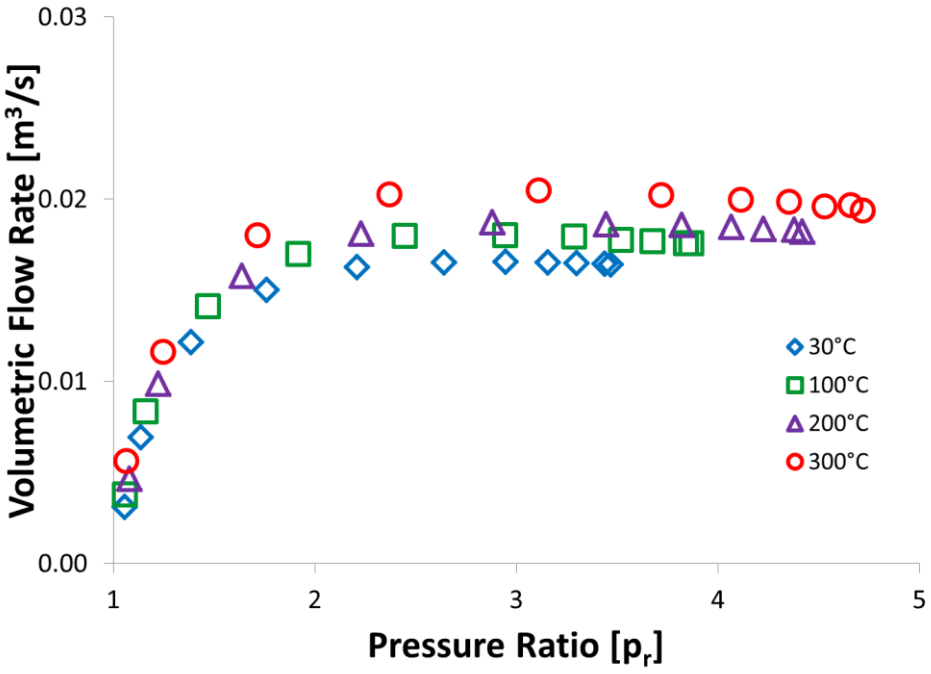

Figure D.1. Labyrinth seal: volumetric flow rate *Q* vs. pressure ratio, $p_r=P_s/P_a$. Non-rotating disk and air at four temperatures (30°C, 100°C, 200°C, and 300°C). Discharge at ambient pressure (P_a).

From simple gas dynamics, the isentropic flow rate through a restriction for an ideal gas is $Q^* = Ac\delta$ where A is the flow area, c is the sound speed, and δ is a modified gas flow function.

The flow area, $A = \pi D C_r$, uses the measured clearance and decreases with increasing temperature due to thermal expansion of the disk mainly. Table 6 details the measured and predicted diametrical clearance for the labyrinth seal at various temperatures.

$$c = \sqrt{\gamma R T_s} \tag{D.1}$$

$$\delta = \frac{\bar{\varphi}}{\sqrt{\gamma}} \tag{D.2}$$

John and Keith [22] define a gas flow function as

$$\varphi = \begin{Bmatrix} \sqrt{\frac{2}{\gamma-1}\left(\frac{\gamma}{R}\right) p_r^{\frac{-(\gamma+1)}{\gamma}} \left(p_r^{\frac{(\gamma-1)}{\gamma}} - 1 \right)} & p_r \le p_{r,choke} \\ \sqrt{\frac{\gamma}{R}\left(\frac{2}{\gamma+1}\right)^{\frac{\gamma+1}{\gamma-1}}} & p_r > p_{r,choke} \end{Bmatrix} \tag{D.3}$$

where

$$\bar{\varphi} = \varphi\sqrt{R} \tag{D.4}$$

Therefore,

$$\bar{\varphi} = \begin{Bmatrix} \sqrt{\frac{2}{\gamma-1}(\gamma) p_r^{\frac{-(\gamma+1)}{\gamma}} \left(p_r^{\frac{(\gamma-1)}{\gamma}} - 1 \right)} & p_r \le p_{r,choke} \\ \sqrt{\gamma\left(\frac{2}{\gamma+1}\right)^{\frac{\gamma+1}{\gamma-1}}} & p_r > p_{r,choke} \end{Bmatrix} \tag{D.5}$$

The dimensionless flow rate, $\bar{Q}$, is found by dividing Q by Q^*

$$\bar{Q} = \frac{Q}{Q^*} = \frac{\dot{m}/\rho}{Ac\delta} \tag{D.6}$$

Figure D.2 shows the dimensionless volumetric flow rate versus pressure ratio for the labyrinth seal. The dimensionless volumetric flow rate remains constant with temperature

after reaching the choke pressure ratio. $\bar{Q}$ shows the volumetric flow rate passing through the labyrinth seal is only 60% of the ideal volumetric flow rate.

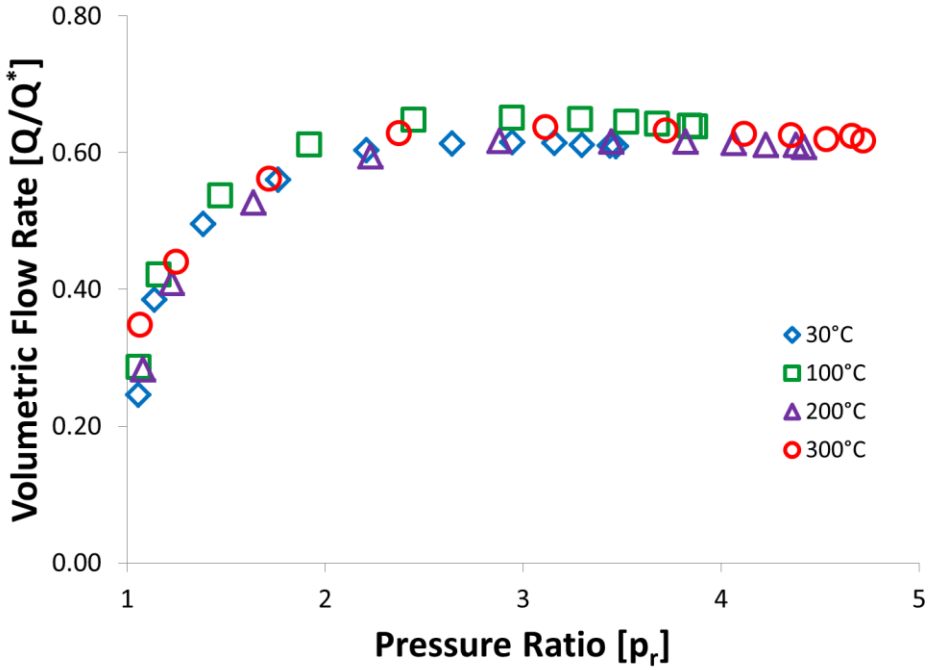

Figure D.2. Labyrinth seal: dimensionless volumetric flow rate $\bar{Q}$ vs. pressure ratio, $p_r=P_s/P_a$. Non-rotating disk and air at four temperatures (30°C, 100°C, 200°C, and 300°C). Discharge at ambient pressure (P_a).